

Design and Kinematic Analysis of a 4-DoF Series-Parallel Hybrid Thumb for Robotic Hands

A Thesis presented

by

Nicholas Baiata

to

The Graduate School

in Partial Fulfillment of the

Requirements

for the Degree of

Master of Science

in

Mechanical Engineering

Robotics

Stony Brook University

May 2025

Stony Brook University

The Graduate School

Nicholas Baiata

We, the thesis committee for the above candidate for the

Master of Science degree, hereby recommend

acceptance of this thesis

Dr. Nilanjan Chakraborty - Thesis Advisor
Associate Professor of the Department of Mechanical Engineering

Dr. Jeffrey Q. Ge
Professor of the Department of Mechanical Engineering

Dr. Amin Fakhari
Assistant Professor of Practice of the Department of Mechanical Engineering

This thesis is accepted by the Graduate School

Celia Marshik
Dean of the Graduate School

Abstract of the Thesis

Design and Kinematic Analysis of a 4-DoF Series-Parallel Hybrid Thumb for Robotic Hands

by

Nicholas Baiata

Master of Science

in

Mechanical Engineering

Robotics

Stony Brook University

2025

This thesis presents a series-parallel hybrid design for a four-degree-of-freedom (4-DoF) thumb and explains why such a design is necessary to achieve an anthropomorphic robotic hand. The only currently available series-parallel hybrid hand features a fixed position, 3-DoF thumb, which results in the loss of open-palm manipulation, less dexterity, and reduces the size of manipulable objects. Previous literature shows that the human thumb has 5-DoFs. However, by analyzing these DoFs, we demonstrate how a 4-DoF mechanism can best approximate human thumb motion. We begin by exploring the anatomical and functional differences between the human thumb and fingers. These differences motivate the design of the 4-DoF thumb, for which a complete kinematic analysis is presented. The forward, inverse, and differential kinematics, along with the Jacobian, are derived to enable full position and velocity control in both joint and task spaces. By projecting the reachable workspaces of the thumb and fingers onto a shared graph, we show how overlap between these appendages enables fine pinching motions, large-object grasps, and open-palm manipulation. The inclusion of an additional DoF in

the thumb also allows for a wider variety of pinch poses, particularly with the index finger. Following the thumb analysis, a detailed design of a modular 3-DoF finger is presented. In this design, minimizing size and simplifying manufacturing were prioritized, while still ensuring high performance from the micromotors, despite cost constraints. These design principles are later extended to the thumb, ensuring consistency in the mechanical design across the hand. Finally, a simplified design of a five-fingered hand (16 DoF) is introduced, and its capabilities for various finger-to-finger and finger-to-thumb interactions are demonstrated through MATLAB Simulink simulations. The resulting design provides a strong foundation for an anthropomorphic, series-parallel driven robotic hand capable of dexterous manipulation, robust grasping, and open-palm tasks.

Contents

List of Abbreviations	x
List of Notations	xi
1 Introduction	1
1.1 Existing Hand/Finger Comparison	4
1.2 Finger Anatomy	8
2 Designing the 4-DoF Thumb	10
2.1 Analysis of the Human Thumb	10
2.2 Forward Kinematics	14
2.2.1 M_1 to q_1	16
2.2.2 M_2 to q_2	16
2.2.3 M_3 to β_1	17
2.2.4 M_4 to β_2	19
2.2.5 β_1 to q_3	20
2.2.6 q_2 and β_2 to β_3	21
2.2.7 q_3 and β_3 to q_4	22
2.2.8 Solving the loop-closure Equations	23
2.2.9 Constructing the Transformation Matrices	24
2.3 Inverse Kinematics	26
2.3.1 End Effector Pose to q_1 and M_1	27
2.3.2 End Effector Pose to q_2 , q_3 , and q_4	27
2.3.3 Finding β_1 , β_2 , and β_3	28
2.3.4 Solving for M_4	28
2.3.5 Solving for M_3	28
2.3.6 Solving for M_2	29
2.4 Differential Kinematics	29
2.4.1 Velocity relation between q_1 and M_1	30
2.4.2 Velocity relation between q_2 and M_1 , M_2	30

2.4.3	Velocity relation between β_1 and M_1, M_2, M_3	31
2.4.4	Velocity relation between β_2 and M_1, M_4	32
2.4.5	Velocity relation between β_3 and M_1, M_2, M_4	33
2.4.6	Velocity relation between q_3 and M_1, M_2, M_3	34
2.4.7	Velocity relation between q_4 and M_2, M_3, M_4	35
2.4.8	Constructing the Jacobian	36
2.5	Kinematic Simulations	39
2.5.1	Path Following	39
2.5.2	Sliding Contact	42
2.5.3	Pivoting Contact	44
3	Detailed Design of the 3-DoF Finger	47
3.1	Finger Structure	48
3.2	Minimum Dimensions and Hardware Selection	49
3.3	Determining Link Dimensions	52
3.3.1	Abduction/Adduction Angle	54
3.4	Final Costing and Size	55
4	Primitive Hand Design	58
4.1	Generating the Workspaces	58
4.2	Satisfying the Design Goals	59
4.3	Hand Simulations	64
5	Conclusions	68
5.1	Future Work	69
	Bibliography	70

List of Figures

1.1	AIDIN Robotics 3-DoF Linkage Driven Finger [31]	7
1.2	Zaw et al. 3-DoF Linkage Driven Finger [51]	8
1.3	Structure of 3-DoF Finger, <i>Partially Adapted From</i> [42]	9
2.1	Diagram of Hand	11
2.2	Anatomical Thumb Convention	12
2.3	Additional Bellcranks in Thumb	13
2.4	Thumb Joint Convention	15
2.5	Origin of Thumb World Frame	15
2.6	q_1 Diagram	16
2.7	M_2 to q_2 Loop	17
2.8	M_3 to β_1 Loop	18
2.9	M_4 to β_2 Loop	19
2.10	β_1 to q_3	20
2.11	β_2 and q_3 to β_3	21
2.12	β_3 and q_3 to q_4 Loop	22
2.13	q_4 to Fingertip	25
2.14	Thumb Tip Position for YZ Planar Motion	40
2.15	Motor Velocities for YZ Planar Motion	40
2.16	Thumb Tip Position for XZ Planar Motion	41
2.17	Motor Velocities for XZ Planar Motion	41
2.18	Thumb Tip Position for Sliding Motion	42
2.19	Motor Velocities for Sliding Motion	43
2.20	Thump Tip Angle during Sliding Motion	43
2.21	Thumb Tip Position for Pivoting Motion	44
2.22	Motor Velocities for Pivoting Motion	45
2.23	Thump Tip Angle during Pivoting Motion	45
3.1	Finger Link Diagram	48

3.2	Finger Joint Diagram	49
3.3	Custom Carriage (threaded inserts in blue)	51
3.4	M_1 Miter Gears and Mounting System	51
3.5	M_2 and M_3 Motor Clamp	52
3.6	Bellcrank (blue) Colliding with a Rod End at $q_1 = 25^\circ$	54
3.7	Detailed Design of 3-DoF Finger	55
3.8	Preliminary Design of 4-DoF Thumb	56
4.1	Workspace of the 3-DoF Finger	59
4.2	Workspace of the 4-DoF Thumb	59
4.3	Workspace of Two Fingers Spaced 30 mm Apart	60
4.4	Side Pinch Simulation, Fingers Spaced 30 mm Apart	61
4.5	Workspace of Two Fingers Spaced 32 mm Apart	61
4.6	Side Pinch Simulation, Fingers Spaced 32 mm Apart	62
4.7	Top Pinch of Two Fingers Spaced 32 mm Apart	62
4.8	Initial Hand Workspace	63
4.9	Final Hand Workspace	64
4.10	Index Finger Motor Velocities during Hand Demonstration . .	64
4.11	Middle Finger Motor Velocities during Hand Demonstration .	65
4.12	Ring Finger Motor Velocities during Hand Demonstration . .	65
4.13	Index Finger Motor Velocities during Hand Demonstration . .	66
4.14	Thumb Motor Velocities during Hand Demonstration	66

List of Tables

1.1	Comparison of Robotic Hands	6
3.1	Bill of Materials for 3-DoF Finger	57

List of Abbreviations

SBU	Stony Brook University
MS	Master of Science
PSS Chain	Prismatic Spherical Spherical Chain
DoF	Degree of Freedom
PCC	Piecewise Constant Curvature
LEAP	Low-cost Efficient AnthroPomorphic Hand
DIY	Do It Yourself
F/T Sensor	Force/Torque Sensor

List of Notations

M or q_2	Scalar
\mathbf{M}	Vector or Matrix
\vec{AO}	Vector on a Linkage
\mathcal{J}	Reference Frame
\mathbf{C}_{q_i}	$\text{Cos}(q_i)$
\mathbf{S}_{q_i}	$\text{Sin}(q_i)$

Chapter 1

Introduction

The goal of modern robotic hand designers is to create a hand capable of both power grasping and fine dexterous manipulation, while maintaining a sleek, compact form factor. Direct-drive, tendon-driven, and linkage-driven fingers are three of the most developed finger types [29]. While underactuated hands are great for power grasping, they simply cannot perform the dexterous motions we are aiming for and therefore will not be discussed much further in this paper [50]. Direct-drive hands are the easiest to control, but they are inherently limited by their motor placement [31]. Larger motors equate to more grasping force, but also larger fingers and less dexterity. Smaller motors grant more dexterity, at the cost of grasping force. Tendon-driven hands solve this issue by moving the motors to the forearm, and actuating the joints via stretchable tendons, such as in the Shadow Robot Dexterous Hand [20]. This results in a very slender hand. However, you cannot push a tendon, so two motors are needed for each degree of freedom. This introduces additional weight, costs, and size (in the forearm). The non-rigid body tendons also introduce more complicated control schemes and dynamics. Linkage-driven hands offer a medium: put the motors in the palm, and actuate the finger with rigid links. This gives slender fingers, with good force output, and one motor per degree of freedom [31]. The major downside is the increased palm thickness, though this is a very reasonable trade-off until better artificial muscles are developed.

The need for dexterous grasping is fairly straightforward, and has been well established [37], [49], [7]. Anytime there are additional constraints associated with a grasping motion, additional degrees of freedom are necessary. These tasks often require in-hand manipulations, so a high DoF arm with a

simple manipulator is not sufficient [37]. This is particularly evident in scenarios where the robot must adjust the position or orientation of an object while maintaining control of it, such as in assembly tasks, handling delicate or irregularly shaped objects, and interacting with environments that lack precise object positioning. Dexterity also equates to adaptability, which is a critical trait in environments where the size and shape of the objects being manipulated vary. In an industrial setting, one might have to be able to lift heavy components, while also being able to manipulate delicate electronics with precision. In a medical setting, one might have to support the weight of a patient while also being able to manipulate a syringe. Before designing the hand, we identified key poses it should be able to perform:

1. The index and middle fingers should be able to perform a side pinch and a top pinch.
2. The thumb should be able to perform a pinch with each finger.
3. The thumb should have multiple pinch positions with the index finger.
4. The hand should have an open palm configuration.

These poses are derived from [19], which outlines 16 common grasp positions, as well as [28], which outlines the Kapandji test, a measure of the opposable dexterity of the thumb. Designing a hand capable of performing all the grips described in [19] and [28] is a significant challenge. To make progress, we introduce an intermediate step by simplifying the required grasps to these four. In addition to being able to hold larger objects, having an open palm configuration is important in the context of a humanoid robot. I would go so far as to say that without an open palm configuration, you wouldn't even have a hand, you would have a claw. The fact that we as humans can achieve an open palm while still performing opposable thumb grasps is one of the reasons why our hands are so efficient. A locked thumb would mean that you are limited by the amount of force that you can apply to the fingers when performing a platform or power push motion [19]. Additionally, in a humanoid robot, if loss of stability occurs, you would want to support yourself using your palms, not your fingers. This response, known as the "Moro Reflex", is a critical indicator that a newborn baby's nervous system is functional [15]. Trying to support a fall with your finger tips could cause enormous damage to the fingers. In order to have an opposable thumb that

can maintain an open palm configuration, special treatment is needed. The human thumb is quite remarkable and has been the subject of extensive research [40]. Compared to the fingers, the thumb has an extra 2-DoF, as well as different phalanges and phalange lengths [12], [25]. Our own workspace analysis shows that longer appendages, a higher adduction/abduction range, and at least one extra degree of freedom is necessary in order to satisfy the previously discussed grasping requirements. The underlying principles used to solve the kinematics for the 3-DoF finger [51] can be extended to the 4-DoF thumb, thus allowing the forward, inverse, and differential kinematics to be solved. A more complete Jacobian is also presented, allowing for control of the thumb's orientation, as well as position, in the task space. Using the kinematics we can simulate position and velocity control in both the joint and task spaces.

While each of the three finger types has their distinct advantages and disadvantages, linkage-driven parallel-series hybrid fingers are among the least researched. The AIDIN hand [31] appears to be the only one currently in production. It is a five-fingered hand where the thumb is simply another 3-DoF finger locked opposite the other four fingers. In [51], an alternate design is proposed for the finger in which the three-dimensional parallel mechanism is collapsed down to two dimensions, thus simplifying the kinematics (see figures 1.1 and 1.2 for comparison). In addition to presenting the kinematics for a 4-DoF thumb, we will also present a detailed design for a 3-DoF finger. The fingers are designed to be modular, with easily removable motors, so that should a motor fail, the entire hand is not rendered useless. Compactness was prioritized over cost, though most parts are 3D-printable and therefore cheap. By far the most expensive components are the micro motors and their controllers, which account for roughly 75% of the cost. While fabricating custom micro motors may be impractical for many researchers, the development of a more cost-effective motor controller presents a more realistic opportunity for reducing overall expenses in the future. Another important criterion when designing the fingers was maintaining the appropriate range of motion for each joint, and ensuring reasonable motor displacements. For example, you would not want to move 10 mm, or 0.001 mm, for a small change in joint position.

In summary, this work begins by outlining the key morphological and functional differences between the human thumb and fingers, motivating the need for a distinct design approach. We then derive the forward, inverse, and differential kinematics for a 4-DoF parallel-series thumb mechanism, en-

abling both positional and orientational control in the task space. A detailed mechanical design is presented for both the modular 3-DoF finger and the 4-DoF thumb, prioritizing compactness, repairability, and manufacturability. Finally, we demonstrate that the proposed hand design is capable of executing a range of dexterous grasping tasks, including opposable thumb interaction and open-palm configurations.

1.1 Existing Hand/Finger Comparison

In this section, we will look at some existing direct-drive, tendon-driven, and linkage-driven hands. Besides their actuation method, we will compare their degrees of freedom, cost, size, force output, and sensing capabilities. Although their actuation method may vary, all hands are composed of rigid links. Soft robotic hands may offer more in terms of compliance, but are much more difficult to model. Finite element methods can be employed, but are much more computationally intensive compared to traditional analytical rigid body dynamics [22]. While fully actuated tendon-driven hands have been historically hard to control, control schemes using joint sensors can be implemented [21] [13]. Although there is prominent new research using piecewise constant curvature (PCC) approximation and partial differential equations to model tendon-driven kinematics, their application in well-established commercial robotics remains limited [32] [4]. PCC models are limited to kinematics, and special treatment is needed to model dynamics [52], while PDEs are notoriously computationally intensive to solve, a major issue in real-time control systems. In our comparison, the Shadow Dexterous Hand [18] will be used to represent the tendon driven hands. They boast 0.2°accuracy in each joint, the most for any high DoF tendon driven robotic hand I could find. The direct-drive hands will be represented by the Allegro [44], Tessolo [46], LEAP [45], and Robotera [23] flagship hands. Allegro, Tessolo, and Robotera are three commercially available robotic hands, while the LEAP hand is an open-source, DIY hand design from researchers at Carnegie Mellon University. There are a myriad of existing direct drive hands from respectable institutions, such as the MIT/UTAH hand, and the DLR Hand 2. However, most of these designs were created long ago using older motor technology. As a result, they tend to be large and heavy, making them unsuitable for the level of dexterous gripping we aim to achieve [10]. Finally, we will compare the AIDIN hand, which served as the main inspiration for

our design. It appears to contain the most developed parallel-series hybrid linkage-driven finger, boasting high force output, positional control through joint sensors, and compact fingers.

Examining Table 1.1, we can clearly see the strengths of each hand type. The direct-drive hands are the cheapest, but also the largest. The tendon-driven hand offers a much smaller form factor, but at a much higher price, and weight. The linkage-driven hand offers fingers similar in size to the tendon-driven hand, but with a weight comparable to that of the direct-drive hands. However, it has the thickest palm and lacks the open palm configuration. Although not the main focus of this paper, the sensing capabilities were included in the comparison to help provide context to the cost of the hands. While there have been many advances in developing low cost, soft, tactile sensors [47] [35] [34], high quality F/T sensors are still rather expensive. In the AIDIN robotics hand, the F/T sensor used retails for \$3,500 [1], while the cost of all other components in the finger is only \sim \$2,400. Additionally, force output is an important metric for robotic manipulators, yet it was omitted from the comparison. This is simply due to the lack of standardization in the way the force output was tested on each hand/finger. The AIDIN group actuated a finger (in a straight and bent position) against a rigid surface until the motors stalled, then measured the force applied to the tip of the finger. The LEAP group oriented the hand palm side up, then pulled down on a fingertip using a force gauge. They then recorded the force when the finger deviated more than 15° from the commanded position. Others, such as the Tesollo and Shadow group, simply list a maximum grip or pinch weight, which is dependent on the friction coefficient at the contact point.

Most importantly, this table shows that no single hand excels in every criterion. The Tesollo hand has the most compact fingers out of all the direct drive hands, but is the heaviest. More importantly, it also lacks fingertip sensorization, the inclusion of which will certainly drive up price and finger size. The LEAP hand is the cheapest option, but also lacks sensorization of the fingertips. The Shadow and AIDIN hands offer compact fingers with sensorization, though at enormous prices, and with complex kinematics. This brings us back to our final goal: design a finger that uses the simpler parallel-series kinematic model, while still maintaining the size and weight of the original. After that, we can extend the mechanical design to the 4-DoF thumb in order to design a linkage driven hand capable of achieving an open palm configuration.

Manuf.	Actuation Method	DoF	# of Fingers	Cost (USD)	Finger Size ¹ (mm)	Hand Size ¹ (mm)	Tactile Sensing	Force/Torque Sensing	Mass (kg)	Open Palm
Allegro	Direct	16	4	\$19,650	28.6x152.7x24.67(28 ²)	139.5x247.7x54.8(28 ³)	Yes	No	1.024	Yes
Tesollo	Direct	20	5	\$15,500	22.4x119x20.5	96.9x215.1x73.5(45 ³)	No	No	1.650	Yes
Leap	Direct	16	4	\$2,000 ⁴	36x150x35(55 ⁵)(20 ²)	140x230x50	No	No	0.595	Yes
Robotera	Direct	12	5	N/A	N/A	94x190.36x47	Yes	No	1.100	Yes
Shadow	Tendon	20	5	\$120,000	20(18 ²)x96x20(22 ²)	86x210x34(22 ³)	Yes	Yes	4.300	Yes
AIDIN	Linkage	15	5	\$50,000	20(17 ²)x101x21.5(14 ²)	110x218x89.5(30.7 ³)	Yes ⁶	Yes	1.100	No

¹ Size format is: width x height x depth.

² Dimension changes at the finger tip.

³ Dimension changes at the base of the finger.

⁴ All other hands have some form of tactile sensing, which this hand lacks. This hand must also be constructed by the user.

⁵ Dimension changes at the proximal phalanx due to the placement of the abduction motor.

⁶ While the fingertip does not have a traditional tactile array, the manufacturers claim tactile sensing capabilities via the F/T sensor and algorithms explored in [6], [33], [30].

Table 1.1: Comparison of Robotic Hands

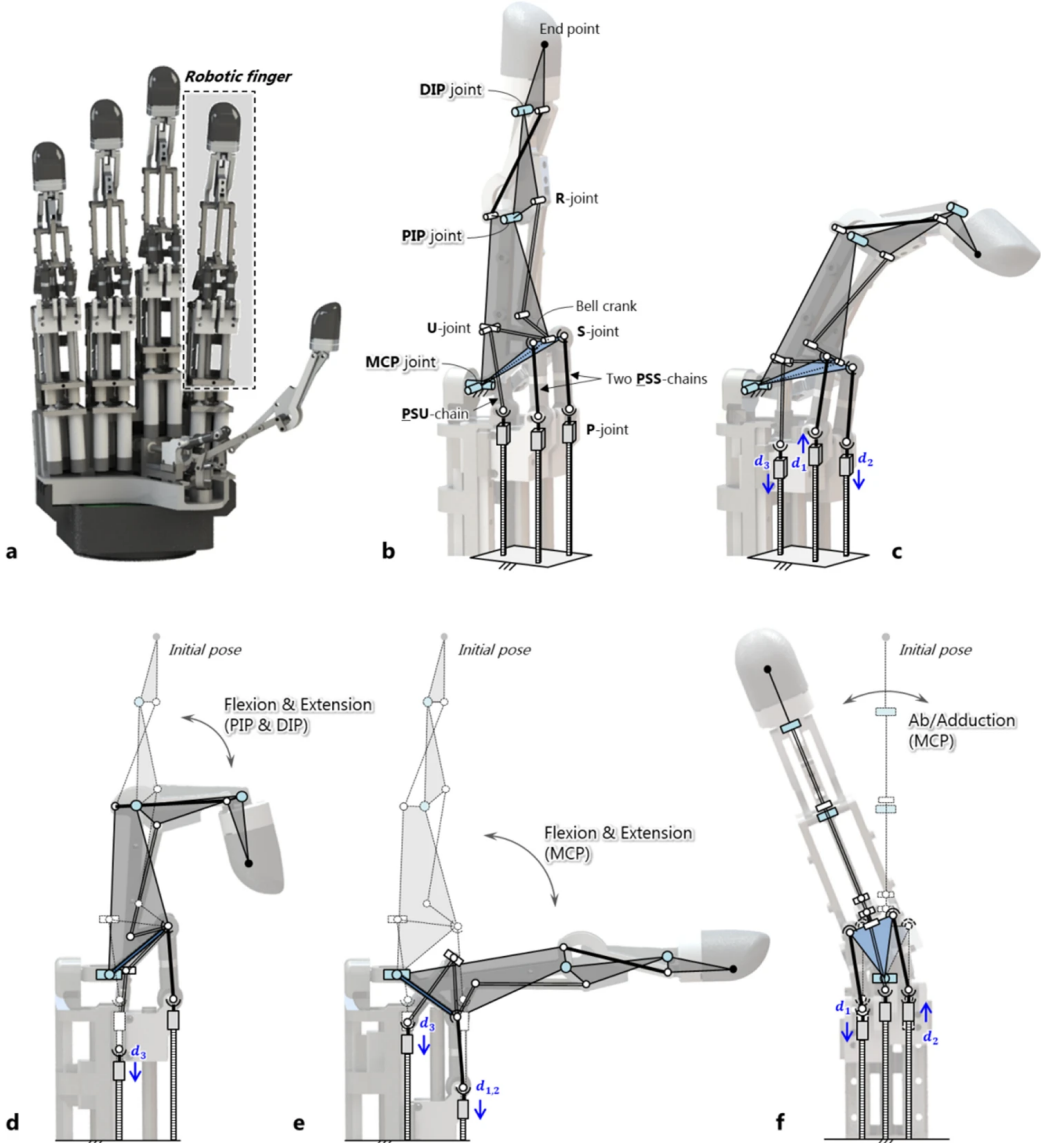


Figure 1.1: AIDIN Robotics 3-DoF Linkage Driven Finger [31]

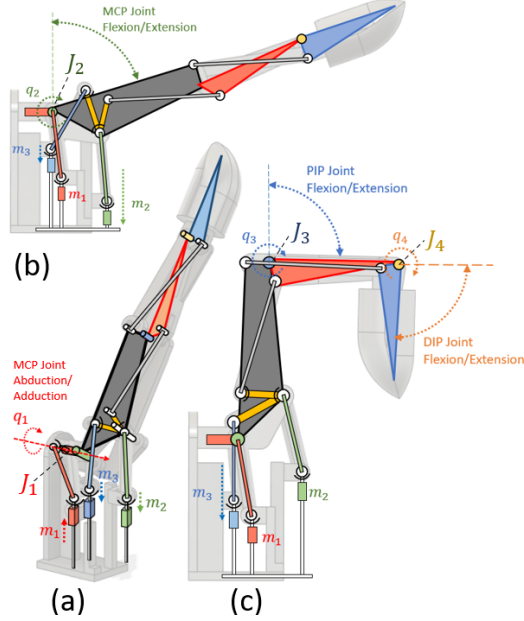


Figure 1.2: Zaw et al. 3-DoF Linkage Driven Finger [51]

1.2 Finger Anatomy

We will briefly turn our attention to the anatomy and naming conventions of the finger, as this terminology will be used throughout the paper. First, we will define abduction/adduction and flexion/extension in this context. Abduction/adduction refers to the side-to-side movement of the finger (commonly referred to as finger *wagging*), while flexion/extension describes the bending and unbending motion of the finger. Figures 1.1 and 1.2 highlight these different motions. For brevity, throughout this paper, the terms 'abduction/adduction' and 'flexion/extension' will be referred to simply as 'abduction' and 'flexion,' respectively. Next, we will examine the anatomy. Starting at the wrist, we have the carpometacarpal (CMC) joints. The CMC joints of the finger are more associated with wrist movements and are typically not considered in robotic finger designs. The same applies to the metacarpal bones, which connect the CMC joints to the metacarpophalangeal (MCP) joints. The MCP joint provides the finger with both abduction and flexion. The proximal phalanx connects the MCP joint to the proximal interphalangeal (PIP) joint. The PIP joint only allows for flexion. The middle (or

intermediate) phalanx connects the PIP joint to the distal interphalangeal (DIP) joint. The DIP joint also only provides flexion motion; however, it is dependent on the motion of the PIP joint (hence, only 3-DoF). Finally, we have the distal phalanx (commonly referred to as the “fingertip”), which is connected to the DIP joint.

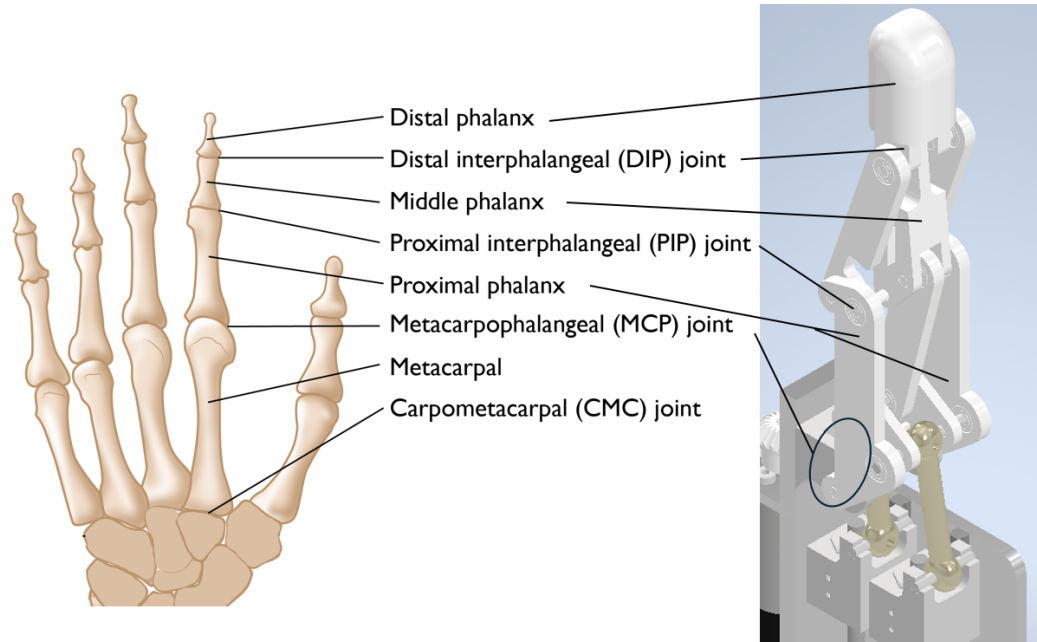


Figure 1.3: Structure of 3-DoF Finger, *Partially Adapted From [42]*

Chapter 2

Designing the 4-DoF Thumb

In this section, we will analyze the human thumb and identify the key differences from the finger. We will then modify the existing series-parallel 3-DoF finger design to fit the new criteria. From there we can solve the forward, inverse, and differential kinematics, as well as present basic motion control using said kinematics. When designing the thumb, it is important to keep the hand design criteria in mind, as the need for opposability and an open palm configuration drives this design.

2.1 Analysis of the Human Thumb

Although the structure of the thumb is similar to that of a finger, there are some key differences [9] [40]:

1. No middle phalanx and PIP joint.
2. Independent control of the IP joint.
3. Approximately 20% longer distal phalanx.
4. A broader, flatter distal phalanx, with a larger "soft tip" region.
5. Abduction in the CMC and MCP joint.

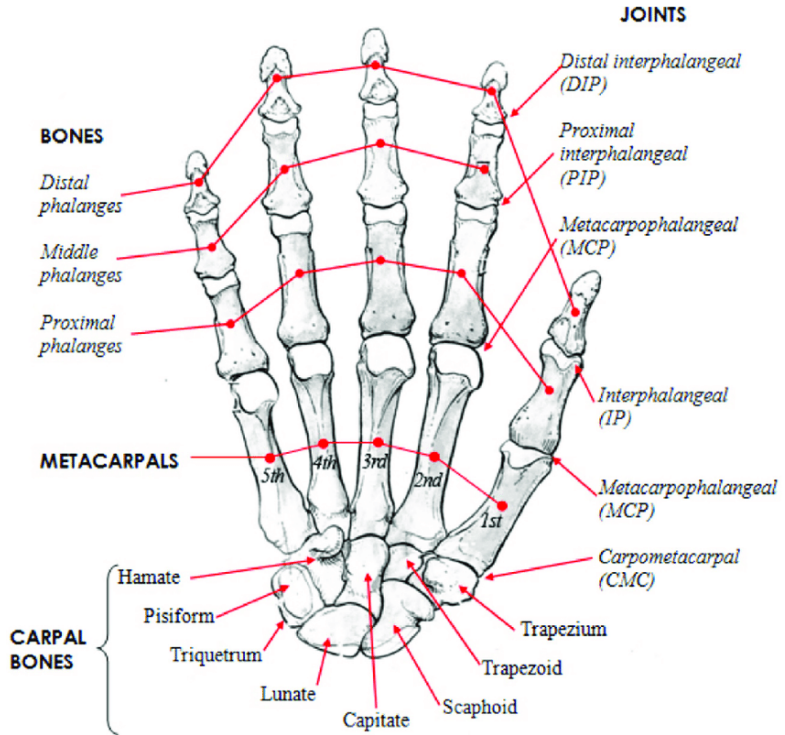


Figure 2.1: Diagram of Hand
[40]

Since the CMC joint and metacarpal bone were not modeled in the 3-DoF finger, item 1 has no real effect on the design, just the naming convention. What was the proximal phalanx now becomes the metacarpal bone, and the middle (or intermediate) phalanx becomes the proximal phalanx. Similarly, the MCP joint becomes the CMC joint, the PIP joint becomes the MCP joint, and the DIP joint becomes the IP joint. Figure 2.2 shows the naming convention. Note: because the CMC joint has both abduction and flexion, it is comprised of two revolute joints with intersecting axes.

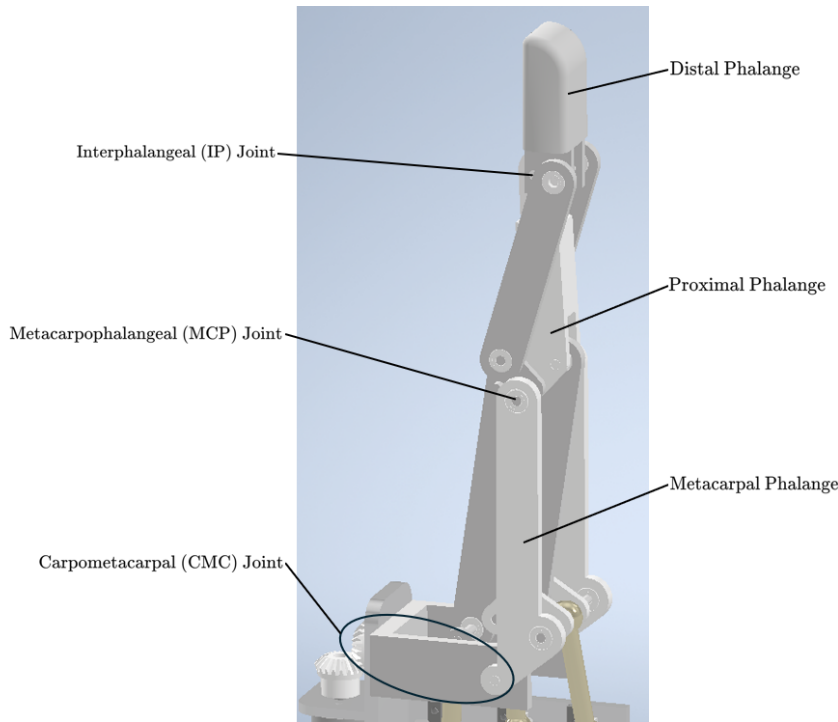


Figure 2.2: Anatomical Thumb Convention

Independent control of the IP joint adds an extra degree of freedom to the mechanism and is critical for in-hand manipulations. It expands the workspace, and allows for multiple pinch positions with each finger. This added degree of freedom is made possible by incorporating two more bellcranks and an additional motor. Technically, the same motion could be achieved using only a single bellcrank, but this would mean having a very long link between the IP joint and the base of the thumb. Figure 2.3 shows the additional bellcranks, linkages, and motor in the thumb design.

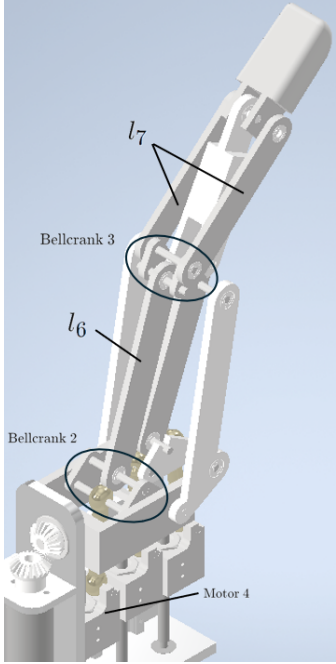


Figure 2.3: Additional Bellcranks in Thumb

Changing the dimensions of the distal phalanx to satisfy 3 and 4 is simple, though its exact dimensions cannot be finalized until it is analyzed within the context of an entire hand. Even still, the design of finger and thumb tips are themselves the topic of extensive research [41] [8]. However, the main focus of this thesis is the kinematics of the thumb and detailed design of the mechanism itself, so the fingertips will be represented by simple anthropomorphic models. Item 5 represents the most difficult challenge in thumb design. Not only is there increased amounts of abduction in the CMC joint, but there is also abduction in the MCP joint [5]. Increasing the abduction in the CMC joint is simple, (as will be discussed in Section 3.3.1) however, introducing abduction in the MCP joint is not. This would require exchanging the bearings at the top of the metacarpals, as well as l_5 and l_6 , for spherical joints. Additionally, the third bellcrank would need to be actuated by another PSS chain. These modifications would significantly increase the size and complexity of the finger, so we will maintain the 4-DoF design and evaluate its performance.

2.2 Forward Kinematics

A critical part of robotic control is the ability to map the motor inputs to the end-effector output. For M_1 , the motor input will be the angle of rotation in radians, where a positive value corresponds to a counter-clockwise abduction motion. For the linear actuators, M_2, M_3, M_4 , the motor inputs are the distance (in mm) each carriage vertically travels from the zero position. These translations occur strictly in the z-axis, but must be embedded into $\mathbf{M}_i \in \mathbb{R}^3$. There are two types of joint angles we solve for: serial and intermediate. The serial joint angles correspond to the actual joint motions of the thumb, where q_1 is the abduction of the CMC joint, q_2 is the flexion of the CMC joint, q_3 is the flexion of the MCP joint, and q_4 is the flexion of the IP joint. The intermediate angles $(\beta_1, \beta_2, \beta_3)$ correspond to the angles of the bellcranks which translate motion from the motors to the serial joints. After relating the motor inputs (M_1, M_2, M_3, M_4) to each serial joint angle (q_1, q_2, q_3, q_4) , we can compose a homogeneous transformation matrix to find the end effector position from the joint angles. For q_2, q_3 and q_4 joint angles of 0° correspond to the unbent positions, and joint angles of -90° correspond to the bent positions. The general procedure for finding these relationships will involve breaking down the mechanism into simpler structures with one unknown, where the loop-closure equations can be solved. In each loop, there will be vectors which describe the distances between joints on certain linkages. Letters will be assigned to each joint, with the vector notation used to describe the vector from one joint to another, i.e., \vec{OA} describes the vector from joint O to joint A . Figure 2.4 shows the convention for each joint. All serial and intermediate joint angles will be assigned reference frames using the calligraphic text, \mathcal{J}_n .

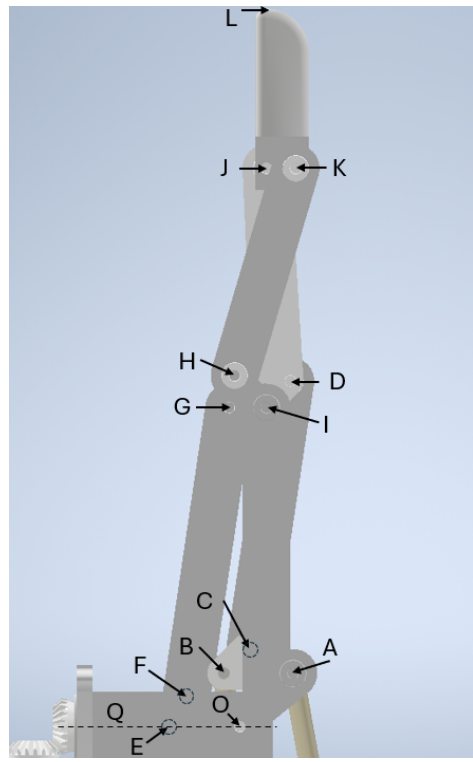


Figure 2.4: Thumb Joint Convention

Additionally, we define the origin of the world frame at the CMC joint, which is the intersection of joints Q and O .

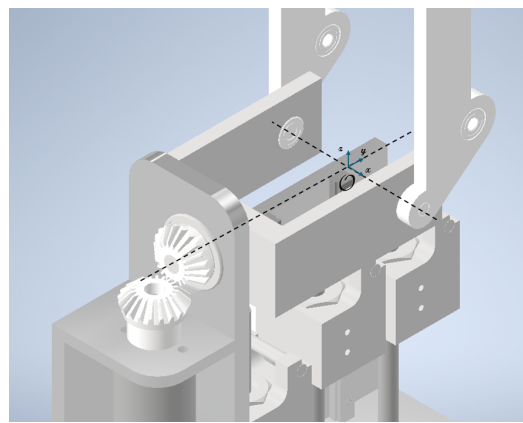


Figure 2.5: Origin of Thumb World Frame

2.2.1 M_1 to q_1

This is the only direct drive joint in the mechanism. Thus, we can directly relate the motor position of M_1 to q_1 and construct the following rotation matrix:

$$\mathbf{R}_{q_1} = \begin{bmatrix} Cq_1 & 0 & Sq_1 \\ 0 & 1 & 0 \\ -Sq_1 & 0 & Cq_1 \end{bmatrix} \quad (2.1)$$

where q_1 is the angle of abduction in the CMC joint. The 'abductor' translates the motion from M_1 to the metacarpals.

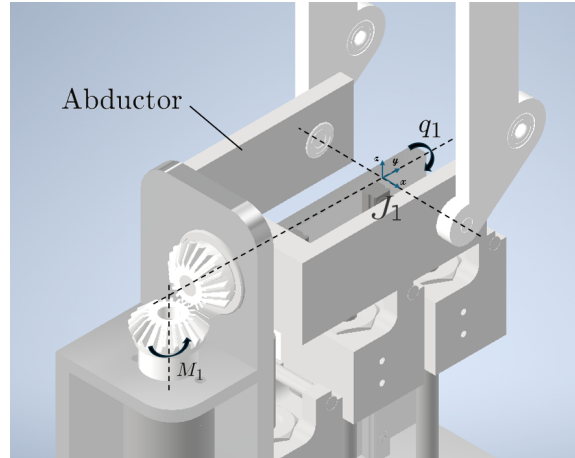


Figure 2.6: q_1 Diagram

2.2.2 M_2 to q_2

Figure 2.7 shows the first loop, which consists of M_2 , that connects to joint A via the PSS chain l_2 . \vec{OA} on the metacarpal linkage connects the abductor to l_2 . The distance between O and M_2 at the zero position is denoted by

\mathbf{P}_2 . The rotation matrix

$$\mathbf{R}_{q_2} = \begin{bmatrix} 1 & 0 & 0 \\ 0 & Cq_2 & -Sq_2 \\ 0 & Sq_2 & Cq_2 \end{bmatrix} \quad (2.2)$$

can be pre-multiplied by \mathbf{R}_{q_1} to give

$$\mathbf{R}_2 = \begin{bmatrix} Cq_1 & Sq_1Sq_2 & Sq_1Cq_2 \\ 0 & Cq_2 & -Sq_2 \\ -Sq_1 & Cq_1Sq_2 & Cq_1Cq_2 \end{bmatrix} \quad (2.3)$$

This yields the first loop-closure equation:

$$l_2 = \mathbf{P}_2 + \mathbf{M}_2 - \mathbf{R}_2 \vec{OA} \quad (2.4)$$

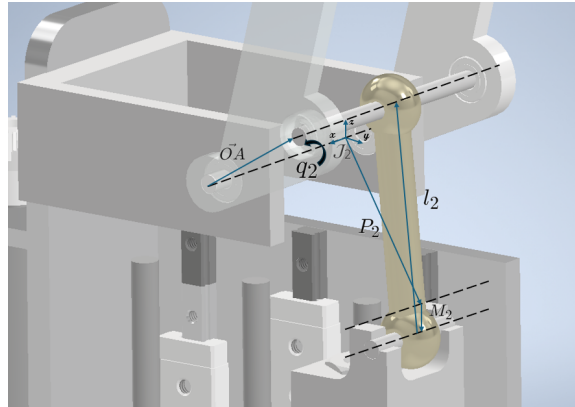


Figure 2.7: M_2 to q_2 Loop

2.2.3 M_3 to β_1

Figure 2.8 shows the second loop, consisting of \mathbf{M}_3 , which connects to the rear joint of the first bellcrank (B) via the PSS chain l_3 . The bellcrank connects

to A via \vec{AB} . Once again, A connects to O via \vec{OA} , and the distance between O and \mathbf{M}_3 at the zero position is \mathbf{P}_3 . The rotation matrix

$$\mathbf{R}_{\beta_1} = \begin{bmatrix} 1 & 0 & 0 \\ 0 & C\beta_1 & -S\beta_1 \\ 0 & S\beta_1 & C\beta_1 \end{bmatrix} \quad (2.5)$$

represents the rotation of the bellcrank at A . Pre-multiplying with the rotations of q_1 and q_2 yields:

$$\mathbf{R}_3 = \begin{bmatrix} Cq_1 & Sq_1S(q_2 + \beta_1) & Sq_1C(q_2 + \beta_1) \\ 0 & C(q_2 + \beta_1) & -S(q_2 + \beta_1) \\ -Sq_1 & Cq_1S(q_2 + \beta_1) & Cq_1C(q_2 + \beta_1) \end{bmatrix} \quad (2.6)$$

which represents the rotation of the first bellcrank, relative to the world frame. This allows us to form the second loop-closure equation:

$$\mathbf{l}_3 = \mathbf{P}_3 + \mathbf{M}_3 - \mathbf{R}_2\vec{OA} - \mathbf{R}_3\vec{AB} \quad (2.7)$$

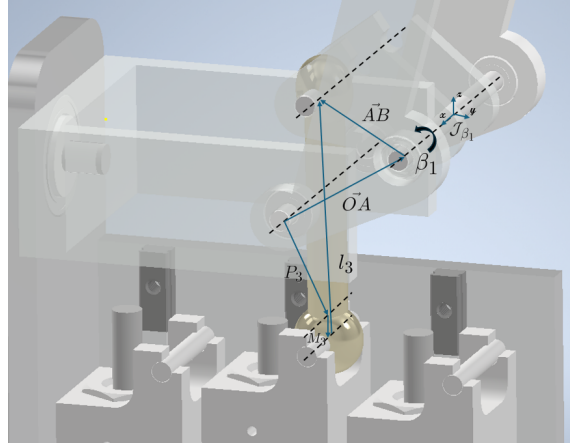


Figure 2.8: \mathbf{M}_3 to β_1 Loop

2.2.4 \mathbf{M}_4 to β_2

Figure 2.9 shows the third loop, consisting of \mathbf{M}_4 , which connects to the rear joint of the second bellcrank (E) via the PSS chain l_4 . The bellcrank connects to O via \vec{OE} and \mathbf{P}_4 represents the distance from O to \mathbf{M}_4 at the zero position. The rotation matrix

$$\mathbf{R}_{\beta_2} = \begin{bmatrix} 1 & 0 & 0 \\ 0 & C\beta_2 & -S\beta_2 \\ 0 & S\beta_2 & C\beta_2 \end{bmatrix} \quad (2.8)$$

represents the rotation of the bellcrank at O . Pre-multiplying by the rotation of q_1 yields:

$$\mathbf{R}_4 = \begin{bmatrix} Cq_1 & Sq_1S\beta_2 & Sq_1C\beta_2 \\ 0 & C\beta_2 & -S\beta_2 \\ -Sq_1 & Cq_1S\beta_2 & Cq_1C\beta_2 \end{bmatrix} \quad (2.9)$$

which represents the rotation of the second bellcrank relative to the world frame. This gives the third loop-closure equation:

$$\mathbf{l}_4 = \mathbf{P}_4 + \mathbf{M}_4 - \mathbf{R}_4 \vec{OE} \quad (2.10)$$

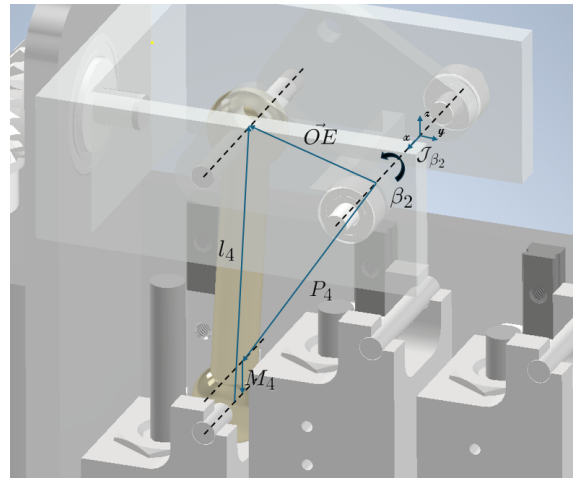


Figure 2.9: \mathbf{M}_4 to β_2 Loop

2.2.5 β_1 to q_3

Figure 2.10 shows the fourth loop, which contains the first bellcrank, the metacarpal, l_5 , and the proximal phalanx. The metacarpal connects to the proximal phalanx via \vec{AI} . The proximal phalanx connects to l_5 via \vec{ID} . l_5 connects to the top of the first bellcrank at C . The front and top joints of the bellcrank are connected via \vec{AC} . The rotation of q_3 about I is represented by the rotation matrix:

$$\mathbf{R}_{q_3} = \begin{bmatrix} 1 & 0 & 0 \\ 0 & C_{q_3} & -S_{q_3} \\ 0 & S_{q_3} & C_{q_3} \end{bmatrix} \quad (2.11)$$

This gives the fourth loop-closure equation:

$$l_5 = -\mathbf{R}_{\beta_1} \vec{AC} + \vec{AI} + \mathbf{R}_{q_2} \mathbf{R}_{q_3} \vec{ID} \quad (2.12)$$

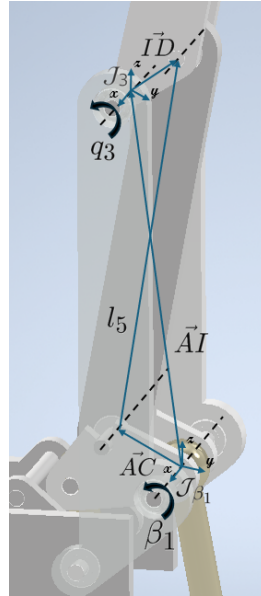


Figure 2.10: β_1 to q_3

2.2.6 q_2 and β_2 to β_3

Figure 2.11 shows the fifth loop, which contains the metacarpal, l_6 , as well as bellcranks two and three. The metacarpal connects the abductor to the third bellcrank via \vec{OI} . The front and back of the third bell are connected via \vec{IG} . The third bellcrank's rear joint is connected to the second bellcrank's top joint via l_6 . The second bellcrank's top and front joints are connected via \vec{OF} . The rotation of β_3 about I is represented by the rotation matrix:

$$\mathbf{R}_{\beta_3} = \begin{bmatrix} 1 & 0 & 0 \\ 0 & C\beta_3 & -S\beta_3 \\ 0 & S\beta_3 & C\beta_3 \end{bmatrix} \quad (2.13)$$

This yields the fifth loop-closure equation:

$$l_6 = -\mathbf{R}_{\beta_2}\vec{OF} + \mathbf{R}_{q_2}\vec{OI} + \mathbf{R}_{\beta_3}\vec{IG} \quad (2.14)$$

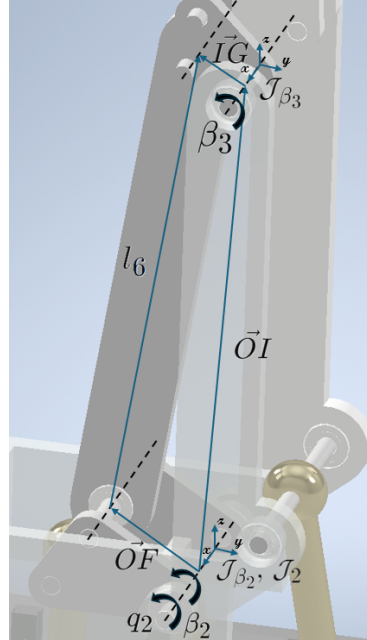


Figure 2.11: β_2 and q_3 to β_3

2.2.7 q_3 and β_3 to q_4

Figure 2.12 shows the sixth and final loop, which contains the proximal and distal phalanges, the third bellcrank, and l_7 . The proximal phalanx connects to the rear joint on the distal phalanx via \vec{IJ} . \vec{JK} represents the distance between the rear and front joints on the distal phalanx. l_7 connects the front joint on the distal phalanx to the top joint on the third bellcrank, H . The front and top joints on the third bellcrank are connected via \vec{IH} . The rotation of q_4 is represented by:

$$\mathbf{R}_{q_4} = \begin{bmatrix} 1 & 0 & 0 \\ 0 & C_{q_4} & -S_{q_4} \\ 0 & S_{q_4} & C_{q_4} \end{bmatrix} \quad (2.15)$$

This yields the sixth and final loop-closure equation:

$$l_7 = -\mathbf{R}_{\beta_3} \vec{IH} + \mathbf{R}_{q_2} \mathbf{R}_{q_3} \vec{IJ} + \mathbf{R}_{q_2} \mathbf{R}_{q_3} \mathbf{R}_{q_4} \vec{JK} \quad (2.16)$$

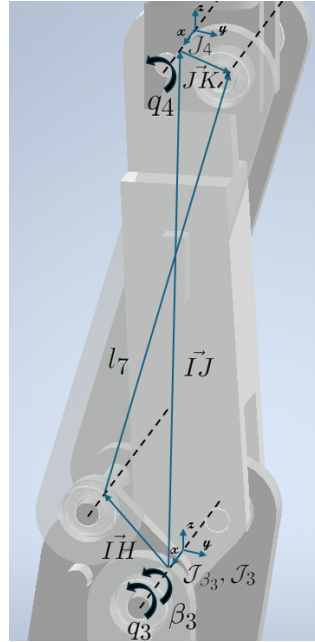


Figure 2.12: β_3 and q_3 to q_4 Loop

2.2.8 Solving the loop-closure Equations

Each loop-closure equation consists of a scalar (l_n), various vectors belonging to \mathbb{R}^3 , some of which are pre-multiplied by rotation matrices in $\text{SO}(3)$, along with the unknown angle. The known vectors and matrices can be simplified to a single vector, which we will call \mathbf{U}_n . The unknown rotation and accompanying vector can be denoted $\mathbf{R}_n \mathbf{V}_n$. By definition of the loop-closure equations, we know the magnitude of \mathbf{U}_n and the unknown rotation, $\mathbf{R}_n \mathbf{V}_n$, must be equal to l_n , i.e.

$$l_n^2 = (\mathbf{U}_n - \mathbf{R}_n \mathbf{V}_n)^T (\mathbf{U}_n - \mathbf{R}_n \mathbf{V}_n) \quad (2.17)$$

Remembering that $\mathbf{R}^T \mathbf{R} = \mathbf{I}$ we can expand the above equation into:

$$l_n^2 = \|\mathbf{U}_n\|^2 + \|\mathbf{V}_n\|^2 + 2\mathbf{U}_n^T \mathbf{R}_n \mathbf{V}_n \quad (2.18)$$

Rearranging the known terms to the right hand side, we get:

$$\mathbf{U}_n^T \mathbf{R}_n \mathbf{V}_n = \frac{\|\mathbf{U}_n\|^2 + \|\mathbf{V}_n\|^2 - l_n^2}{2} \quad (2.19)$$

The right-hand side of this equation will be denoted by S_n . Multiplying out the left-hand side will yield a long polynomial, which can then be simplified to the following form:

$$A_n \sin(q_n) + B_n \cos(q_n) + C_n = 0 \quad (2.20)$$

where C_n includes S_n , along with any other constants resulting from the multiplication of the left hand side. The solution to this equation is a known trigonometric problem and is given here:

$$q_n = \arctan 2(A_n, B_n) \pm \arccos \left(\frac{-C_n}{\sqrt{A_n^2 + B_n^2}} \right) \quad (2.21)$$

Let us look at the first equation, (2.4). In this case

$$\mathbf{U}_2 = \mathbf{P}_2 + \mathbf{M}_2 \quad (2.22)$$

While each vector has 3 components, we can save time by recognizing that there are some components that will always be zero, regardless of the link dimensions or motor inputs. First, we know that the motors can only move

up and down, meaning M_{2x} and M_{2y} will always be zero. Second, we know that all linkages are planar, so P_{2y} and AO_y are also zero. This gives us:

$$\mathbf{U}_2 = \begin{bmatrix} P_{2x} \\ 0 \\ P_{2z} + M_{2z} \end{bmatrix} \quad (2.23)$$

and

$$\vec{AO} = \begin{bmatrix} AO_x \\ 0 \\ AO_z \end{bmatrix} = \mathbf{V}_2 = \begin{bmatrix} V_{2x} \\ 0 \\ V_{2z} \end{bmatrix} \quad (2.24)$$

Expanding the left hand side of (2.19) we get:

$$A_2 = V_{2z}P_{2x} - V_{2x}(M_{2z} + P_{2z})\cos(q_1) \quad (2.25)$$

$$B_2 = V_{2x}P_{2x} + V_{2z}(M_{2z} + P_{2z})\cos(q_1) \quad (2.26)$$

$$C_n = -S_n \quad (2.27)$$

Each equation can be solved for using the same steps, resulting in q_2 , q_3 , q_4 , β_1 , β_2 , and β_3 .

2.2.9 Constructing the Transformation Matrices

Using the joint rotations of q_1 , q_2 , q_3 , q_4 , and the appropriate link lengths, we can treat the thumb as a serial manipulator and construct homogeneous transformation matrices. This will allow us to calculate the end-effector location for a given set of motor inputs. However, we still need to introduce a frame at the fingertip, \mathcal{J}_{EE} . Figure 2.13 shows this final reference frame, located at the end of \bar{JK} , and rotated by the angle q_4 .

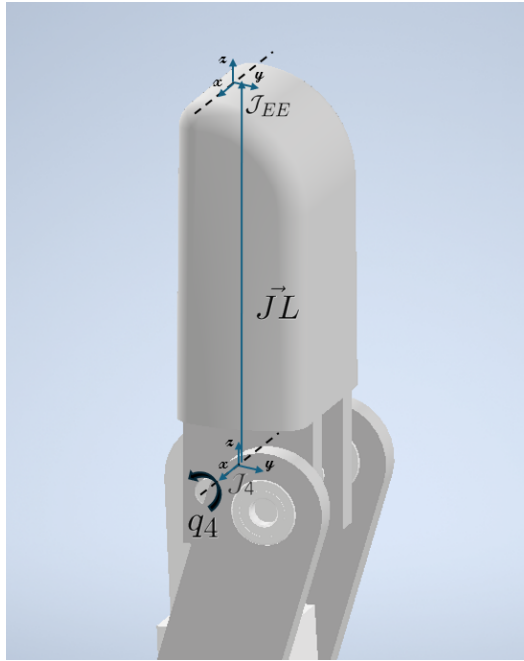


Figure 2.13: q_4 to Fingertip

$$T_{\mathcal{O}}^{\mathcal{J}_1} = \begin{bmatrix} Cq_1 & 0 & Sq_1 & 0 \\ 0 & 1 & 0 & 0 \\ -Sq_1 & 0 & Cq_1 & 0 \\ 0 & 0 & 0 & 1 \end{bmatrix} \quad (2.28)$$

$$T_{\mathcal{J}_1}^{\mathcal{J}_2} = \begin{bmatrix} 1 & 0 & 0 & 0 \\ 0 & Cq_2 & -Sq_2 & 0 \\ 0 & Sq_2 & Cq_2 & 0 \\ 0 & 0 & 0 & 1 \end{bmatrix} \quad (2.29)$$

$$T_{\mathcal{J}_2}^{\mathcal{J}_3} = \begin{bmatrix} 1 & 0 & 0 & 0 \\ 0 & Cq_3 & -Sq_3 & OI_y \\ 0 & Sq_3 & Cq_3 & OI_z \\ 0 & 0 & 0 & 1 \end{bmatrix} \quad (2.30)$$

$$T_{\mathcal{J}_3}^{\mathcal{J}_4} = \begin{bmatrix} 1 & 0 & 0 & 0 \\ 0 & Cq_4 & -Sq_4 & IJ_y \\ 0 & Sq_4 & Cq_4 & IJ_z \\ 0 & 0 & 0 & 1 \end{bmatrix} \quad (2.31)$$

$$T_{\mathcal{J}_4}^{\mathcal{J}_{EE}} = \begin{bmatrix} 1 & 0 & 0 & 0 \\ 0 & 1 & 0 & 0 \\ 0 & 0 & 1 & JL_z \\ 0 & 0 & 0 & 1 \end{bmatrix} \quad (2.32)$$

$$T_{\mathcal{O}}^{\mathcal{J}_{EE}} = T_{\mathcal{O}}^{\mathcal{J}_1} T_{\mathcal{J}_1}^{\mathcal{J}_2} T_{\mathcal{J}_2}^{\mathcal{J}_3} T_{\mathcal{J}_3}^{\mathcal{J}_4} T_{\mathcal{J}_4}^{\mathcal{J}_{EE}} \quad (2.33)$$

2.3 Inverse Kinematics

We will now analyze the positional inverse kinematics (IK) of the mechanism. Finding the inverse kinematics of any robotic mechanism is important as it allows planning in the task space. This is useful when an object in the task space must be avoided, or a deliberate grip needs to be deployed. Finding q_1 (and subsequently \mathbf{M}_1) is straightforward, as any displacement in the x-axis is due to this rotation. The method for finding the planar joint angles (q_2, q_3, q_4) is also straightforward, as 3-DoF planar serial manipulators are well understood. From there, we will need to use the loop-closure equations to find the values of β_1, β_2 , and β_3 , followed by $\mathbf{M}_2, \mathbf{M}_3$, and \mathbf{M}_4 .

Because the thumb has 4-DoF, the end-effector location alone is not enough to fully describe the mechanism. The pose of the end-effector must

be given, specifically, the angle of the distal phalanx in the YZ plane, since this corresponds to the fourth degree of freedom. The desired end-effector location will be referred to as $\mathbf{EE} = [EE_x, EE_y, EE_z]$, with a desired distal phalanx angle (relative to the global frame) α .

2.3.1 End Effector Pose to q_1 and M_1

As previously stated, any displacement along the x-axis is a result of the rotation at q_1 , as such:

$$q_1 = \arctan 2(EE_x, EE_z) \quad (2.34)$$

From there, the desired location is multiplied by

$$R = \begin{bmatrix} Cq_1 & 0 & -Sq_1 \\ 0 & 1 & 0 \\ Sq_1 & 0 & Cq_1 \end{bmatrix} \quad (2.35)$$

in order to *un-rotate* the mechanism and get the desired location in the YZ plane. This will make the subsequent calculations easier as the mechanism will be simplified to a 2-D problem.

2.3.2 End Effector Pose to q_2, q_3 , and q_4

We now have a 3R planar serial manipulator, the solution to which is well-known. First, we denote the following: $d_1 = \|\vec{OI}\|$, $d_2 = \|\vec{IJ}\|$, $d_3 = \|\vec{JL}\|$. Using α , we can find the coordinates of the third joint (J) in the YZ plane:

$$y = EE_y - d_3 \sin(\alpha) \quad (2.36)$$

$$z = EE_z - d_3 \cos(\alpha) \quad (2.37)$$

We have now simplified the problem to the 2R planar case where (y, z) is the location of the end effector, with d_1 and d_2 as the link lengths. Using the method from [36], we get q_2 and q_3 . It is important to note this method returns two sets of angles, the *lefty* and the *righty* solutions. Because of the range of motion of the joints we must always select the 'lefty' solution. From here, q_4 can be calculated as:

$$q_4 = \alpha - q_3 - q_2 \quad (2.38)$$

2.3.3 Finding β_1 , β_2 , and β_3

In order to find β_1 , β_2 , and β_3 , we must solve the appropriate loop-closure equations from the previous section. Since q_2 , q_3 , and q_4 are known, we can solve Equation 2.16 for β_3 , Equation 2.14 for β_2 , and Equation 2.12 for β_1 . Employing the same method from Section 2.1.8 will yield β_1 , β_2 , and β_3 .

2.3.4 Solving for \mathbf{M}_4

Using Equation 2.10 we can solve for \mathbf{M}_4 since q_1 and β_2 are now known. We denote the known vectors as \mathbf{W}_n , in this case

$$\mathbf{W}_4 = \mathbf{P}_4 - \mathbf{R}_4 \vec{OE} = \begin{bmatrix} W_{4x} \\ W_{4y} \\ W_{4z} \end{bmatrix} \quad (2.39)$$

Which gives the loop-closure equation:

$$l_4 = \mathbf{W}_4 + \mathbf{M}_4 \quad (2.40)$$

Once again we can set the magnitudes equal to each other:

$$l_4^2 = W_{4x}^2 + W_{4y}^2 + (W_{4z} + M_{4z})^2 \quad (2.41)$$

Then solve for \mathbf{M}_4 :

$$M_4 = \sqrt{l_4^2 - W_{4x}^2 - W_{4y}^2} - W_{4z} \quad (2.42)$$

2.3.5 Solving for \mathbf{M}_3

Using Equation 2.7 we can solve for \mathbf{M}_3 since q_1 , q_2 , and β_1 are known. In this case:

$$\mathbf{W}_3 = \mathbf{P}_3 - \mathbf{R}_2 \vec{OA} - \mathbf{R}_3 \vec{AB} = \begin{bmatrix} W_{3x} \\ W_{3y} \\ W_{3z} \end{bmatrix} \quad (2.43)$$

which gives the following loop-closure equation:

$$l_3 = \mathbf{W}_3 + \mathbf{M}_3 \quad (2.44)$$

We can then solve for \mathbf{M}_3 using the same process shown in Equations 2.41 and 2.42.

2.3.6 Solving for \mathbf{M}_2

Using Equation 2.4 we can solve for \mathbf{M}_2 since q_1 and q_2 are known. In this case:

$$\mathbf{W}_2 = \mathbf{P}_2 - \mathbf{R}_2 \vec{OA} = \begin{bmatrix} W_{2x} \\ W_{2y} \\ W_{2z} \end{bmatrix} \quad (2.45)$$

which gives the following loop-closure equation:

$$l_2 = \mathbf{W}_2 + \mathbf{M}_2 \quad (2.46)$$

Once again we can solve for \mathbf{M}_2 using the process shown in Equations 2.41 and 2.42.

2.4 Differential Kinematics

We will now analyze the mechanism's differential kinematics. This will involve finding the relationships between the motor velocities and the angular velocities of the joints. From there we can build the Jacobian and relate the end-effector velocity to the motor velocities. This will allow us to perform Resolved Rate Motion Control [48], a control scheme that moves the end effector smoothly from one point to another within the task space at a desired velocity. This relationship is given in Equation 2.47, where $d\mathbf{M}$ is a 4x1 vector of motor velocities, \mathbf{J} is the Jacobian (6x4), and $d\mathbf{X}$ is a 6x1 vector of end effector velocities. In this case $d\mathbf{X}$ would contain the velocities in the x, y, and z directions, as well as the angular velocities about each axis.

$$d\mathbf{M} = \mathbf{J}^{-1} d\mathbf{X} \quad (2.47)$$

By iteratively entering velocities for specified amounts of time, we can generate the necessary motor displacements to achieve our desired path.

2.4.1 Velocity relation between q_1 and M_1

Since q_1 is direct-drive, we assume:

$$\frac{\partial q_1}{\partial M_1} = 1 \quad (2.48)$$

Note this value could vary depending on the gear ratio between the motor and the joint, though it will always remain constant for a given configuration. Here, we will choose 1 for simplicity.

2.4.2 Velocity relation between q_2 and M_1, M_2

We begin again with the first loop-closure equation, (2.4). From there, we organize the terms in the same procedure outlined in (2.17), denoting \vec{OA} as \mathbf{V}_2 . Expanding the right-hand side, we get:

$$\begin{aligned} l_2^2 &= [P_{2x} - V_{2x}Cq_2 - V_{2z}Sq_2]^2 \\ &\quad + [V_{2x}Sq_1Sq_2 - V_{2z}Sq_1Cq_2]^2 \\ &\quad + [P_{2z} + M_2 - V_{2z}Cq_1Cq_2 + V_{2x}Cq_1Sq_2]^2 \end{aligned} \quad (2.49)$$

In order to take the derivative with respect to M_1 and M_2 we apply the chain rule and find the partial derivatives for the intermediate variables q_1 , q_2 , and M_2 . For clarity, we will set the terms on the right-hand side equal to the following:

$$A_2 = P_{2x} - V_{2x}Cq_2 - V_{2z}Sq_2 \quad (2.50)$$

$$B_2 = V_{2x}Sq_1Sq_2 - V_{2z}Sq_1Cq_2 \quad (2.51)$$

$$C_2 = P_{2z} + M_2 - V_{2z}Cq_1Cq_2 + V_{2x}Cq_1Sq_2 \quad (2.52)$$

Taking the partial derivative of (2.49) with respect to q_1 gives:

$$D_2 = B_2(V_{2x}Cq_1Sq_2 - V_{2z}Cq_1Cq_2) + C_2(V_{2z}Sq_1Cq_2 - V_{2x}Sq_1Sq_2) \quad (2.53)$$

Taking the partial derivative of (2.49) with respect to q_2 gives:

$$E_2 = A_2(V_{2x}Sq_2 - V_{2z}Cq_2) + B_2(V_{2x}Sq_1Cq_2 + V_{2z}Sq_1Sq_2) + C_2(V_{2z}Cq_1Sq_2 + V_{2x}Cq_1Cq_2) \quad (2.54)$$

The partial derivative of (2.49) with respect to M_2 is simply C_2 . We can now relate q_2 to M_i for $i = 1, 2$

$$0 = E_2 \frac{\partial q_2}{\partial M_i} + D_2 \frac{\partial q_1}{\partial M_i} + C_2 \frac{\partial M_2}{\partial M_i} \quad (2.55)$$

$\frac{\partial M_2}{\partial M_1} = \frac{\partial q_1}{\partial M_2} = 0$, resulting in:

$$\frac{\partial q_2}{\partial M_1} = -\frac{D_2}{E_2} \frac{\partial q_1}{\partial M_1} \quad (2.56)$$

$$\frac{\partial q_2}{\partial M_2} = \frac{-C_2}{E_2} \quad (2.57)$$

2.4.3 Velocity relation between β_1 and M_1, M_2, M_3

Using the second loop-closure equation (2.7), we denote \vec{AB} as \mathbf{V}_3 . Setting the magnitudes of the vectors and scalar equal, we get:

$$\begin{aligned} l_3^2 &= [P_{3x} - V_{2x}Cq_2 - V_{2z}Sq_2 - V_{3x}C(q_2 + \beta_1) - V_{3z}S(q_2 + \beta_1)]^2 \\ &\quad + [V_{2x}Sq_1Sq_2 - V_{2z}Sq_1Cq_2 + V_{3x}Sq_1S(q_2 + \beta_1) - V_{3z}Sq_1C(q_2 + \beta_1)]^2 \\ &\quad + [P_{3z} + M_3 - V_{2z}Cq_1Cq_2 + V_{2x}Cq_1Sq_2 - V_{3z}Cq_1C(q_2 + \beta_1) + V_{3x}Cq_1S(q_2 + \beta_1)]^2 \end{aligned} \quad (2.58)$$

Once again we will organize the terms into the following:

$$A_3 = P_{3x} - V_{2x}Cq_2 - V_{2z}Sq_2 - V_{3x}C(q_2 + \beta_1) - V_{3z}S(q_2 + \beta_1) \quad (2.59)$$

$$B_3 = V_{2x}Sq_1Sq_2 - V_{2z}Sq_1Cq_2 + V_{3x}Sq_1S(q_2 + \beta_1) - V_{3z}Sq_1C(q_2 + \beta_1) \quad (2.60)$$

$$C_3 = P_{3z} + M_3 - V_{2z}Cq_1Cq_2 + V_{2x}Cq_1Sq_2 - V_{3z}Cq_1C(q_2 + \beta_1) + V_{3x}Cq_1S(q_2 + \beta_1) \quad (2.61)$$

The partial derivative of (2.58) with respect to q_1 is:

$$\begin{aligned} D_3 &= B_3(V_{2x}Cq_1Sq_2 - V_{2z}Cq_1Cq_2 + V_{3x}Cq_1S(q_2 + \beta_1) - V_{3z}Cq_1C(q_2 + \beta_1)) \\ &\quad + C_3(V_{2z}Sq_1Cq_2 - V_{2x}Sq_1Sq_2 + V_{3z}Sq_1C(q_2 + \beta_1) - V_{3x}Sq_1S(q_2 + \beta_1)) \end{aligned} \quad (2.62)$$

The partial derivative of (2.58) with respect to q_2 is:

$$\begin{aligned} E_3 &= A_3(V_{2x}Sq_2 - V_{2z}Cq_2 + V_{3x}S(q_2 + \beta_1) - V_{3z}C(q_2 + \beta_1)) \\ &\quad + B_3(V_{2x}Sq_1Cq_2 + V_{2z}Sq_1Sq_2 + V_{3x}Sq_1C(q_2 + \beta_1) + V_{3z}Sq_1S(q_2 + \beta_1)) \\ &\quad + C_3(V_{2z}Cq_1Sq_2 + V_{2x}Cq_1Cq_2 + V_{3z}Cq_1S(q_2 + \beta_1) + V_{3x}Cq_1C(q_2 + \beta_1)) \end{aligned} \quad (2.63)$$

The partial derivative of (2.58) with respect to β_1 is:

$$\begin{aligned} F_3 = & A_3(V_{3x}S(q_2 + \beta_1) - V_{3z}C(q_2 + \beta_1)) \\ & + B_3(V_{3x}Sq_1C(q_2 + \beta_1) + V_{3z}Sq_1S(q_2 + \beta_1)) \\ & + C_3(V_{3z}Cq_1S(q_2 + \beta_1) + V_{3x}Cq_1C(q_2 + \beta_1)) \end{aligned} \quad (2.64)$$

And again the partial derivative of (2.58) with respect to M_3 is C_3 . The relation between β_1 and M_i for $i = 1, 2, 3$ is shown below.

$$0 = E_3 \frac{\partial q_2}{\partial M_i} + D_3 \frac{\partial q_1}{\partial M_i} + F_3 \frac{\partial \beta_1}{\partial M_i} + C_3 \frac{\partial M_3}{\partial M_i} \quad (2.65)$$

$\frac{\partial M_3}{\partial M_1} = \frac{\partial M_3}{\partial M_2} = \frac{\partial q_1}{\partial M_3} = \frac{\partial q_2}{\partial M_3} = \frac{\partial q_1}{\partial M_3} = 0$, which gives:

$$\frac{\partial \beta_1}{\partial M_1} = -\frac{E_3}{F_3} \frac{\partial q_2}{\partial M_1} - \frac{D_3}{F_3} \frac{\partial q_1}{\partial M_1} \quad (2.66)$$

$$\frac{\partial \beta_1}{\partial M_2} = -\frac{E_3}{F_3} \frac{\partial q_2}{\partial M_2} \quad (2.67)$$

$$\frac{\partial \beta_1}{\partial M_3} = -\frac{C_3}{F_3} \quad (2.68)$$

2.4.4 Velocity relation between β_2 and M_1, M_4

Using the third loop-closure equation (2.10) we denote \vec{OE} as \mathbf{V}_4 . Setting the magnitudes of the vectors and scalar equal we get:

$$\begin{aligned} l_4^2 = & [P_{4x} - V_{4x}C\beta_2 - V_{4z}S\beta_2]^2 \\ & + [V_{4x}Sq_1S\beta_2 - V_{4z}Sq_1C\beta_2]^2 \\ & + [P_{4z} + M_4 - V_{4z}Cq_1C\beta_2 + V_{4x}Cq_1S\beta_2]^2 \end{aligned} \quad (2.69)$$

Organizing the right hand side terms:

$$A_4 = P_{4x} - V_{4x}C\beta_2 - V_{4z}S\beta_2 \quad (2.70)$$

$$B_4 = V_{4x}Sq_1S\beta_2 - V_{4z}Sq_1C\beta_2 \quad (2.71)$$

$$C_4 = P_{4z} + M_4 - V_{4z}Cq_1C\beta_2 + V_{4x}Cq_1S\beta_2 \quad (2.72)$$

Taking the partial derivative of (2.78) with respect to q_1 gives:

$$D_4 = B_4(V_{4x}Cq_1S\beta_2 - V_{4z}Cq_1C\beta_2) + C_4(V_{4z}Sq_1C\beta_2 - V_{4x}Sq_1S\beta_2) \quad (2.73)$$

Taking the partial derivative of (2.78) with respect to β_2 gives:

$$E_4 = A_4(V_{4x}S\beta_2 - V_{4z}C\beta_2) + B_4(V_{4x}Sq_1C\beta_2 + V_{4z}Sq_1S\beta_2) + C_4(V_{4z}Cq_1S\beta_2 + V_{4x}Cq_1C\beta_2) \quad (2.74)$$

Again the partial derivative of (2.78) with respect to M_4 is simply C_4 . The relation between β_2 and M_i for $i = 1, 4$ is shown below:

$$0 = E_4 \frac{\partial \beta_2}{\partial M_i} + D_4 \frac{\partial q_1}{\partial M_i} + C_4 \frac{\partial M_4}{\partial M_i} \quad (2.75)$$

$\frac{\partial M_4}{\partial M_1} = \frac{\partial q_1}{\partial M_4} = 0$, resulting in:

$$\frac{\partial \beta_2}{\partial M_1} = -\frac{D_2}{E_2} \frac{\partial q_1}{\partial M_1} \quad (2.76)$$

$$\frac{\partial \beta_2}{\partial M_4} = -\frac{C_4}{E_4} \quad (2.77)$$

2.4.5 Velocity relation between β_3 and M_1, M_2, M_4

Using the fifth loop-closure equation (2.14) we denote \vec{OI} as \mathbf{V}_5 , \vec{OF} as \mathbf{V}_6 , and \vec{IG} , as \mathbf{V}_7 . Setting the magnitudes of the vectors and scalar equal we get:

$$l_6^2 = [V_{5x}Cq_2 - V_{6x}C\beta_2 + V_{7x}C\beta_3 + V_{5z}Sq_2 - V_{6z}S\beta_2 + V_{7z}S\beta_3]^2 + [V_{5z}Cq_2 - V_{6z}C\beta_2 + V_{7z}C\beta_3 - V_{5x}Sq_2 + V_{6x}S\beta_2 - V_{7x}S\beta_3]^2 \quad (2.78)$$

Organizing the right hand side terms:

$$A_5 = V_{5x}Cq_2 - V_{6x}C\beta_2 + V_{7x}C\beta_3 + V_{5z}Sq_2 - V_{6z}S\beta_2 + V_{7z}S\beta_3 \quad (2.79)$$

$$B_5 = V_{5z}Cq_2 - V_{6z}C\beta_2 + V_{7z}C\beta_3 - V_{5x}Sq_2 + V_{6x}S\beta_2 - V_{7x}S\beta_3 \quad (2.80)$$

The partial derivative of (2.78) with respect to q_2 is:

$$D_5 = A_5(-V_{5x}Sq_2 + V_{5z}Cq_2) + B_5(-V_{5z}Sq_2 - V_{5x}Cq_2) \quad (2.81)$$

The partial derivative of (2.78) with respect to β_2 is:

$$E_5 = A_5(V_{6x}S\beta_2 - V_{6z}C\beta_2) + B_5(V_{6z}S\beta_2 + V_{6x}C\beta_2) \quad (2.82)$$

The partial derivative of (2.78) with respect to β_3 is:

$$F_5 = A_5(-V_{7x}S\beta_3 + V_{7z}C\beta_3) + B_5(-V_{7z}S\beta_3 - V_{7x}C\beta_3) \quad (2.83)$$

The relation between β_3 and M_i for $i = 1, 2, 4$ is:

$$0 = F_5 \frac{\partial \beta_3}{\partial M_i} + D_5 \frac{\partial q_2}{\partial M_i} + E_5 \frac{\partial \beta_2}{\partial M_i} \quad (2.84)$$

$\frac{\partial \beta_2}{\partial M_2} = \frac{\partial q_2}{\partial M_4} = 0$, resulting in:

$$\frac{\partial \beta_3}{\partial M_1} = -\frac{D_5}{F_5} \frac{\partial q_2}{\partial M_1} - \frac{E_5}{F_5} \frac{\partial \beta_2}{\partial M_1} \quad (2.85)$$

$$\frac{\partial \beta_3}{\partial M_2} = -\frac{D_5}{F_5} \frac{\partial q_2}{\partial M_2} \quad (2.86)$$

$$\frac{\partial \beta_3}{\partial M_2} = -\frac{E_5}{F_5} \frac{\partial \beta_2}{\partial M_4} \quad (2.87)$$

2.4.6 Velocity relation between q_3 and M_1, M_2, M_3

Using the fourth loop-closure equation (2.12), we denote \vec{AI} as \mathbf{V}_8 , \vec{AC} as \mathbf{V}_9 , and \vec{ID} as \mathbf{V}_{10} .

$$\begin{aligned} l_6^2 &= [V_{8x} - V_{9x}C(\beta_1 - q_2) + V_{10x}Cq_3 - V_{9z}S(\beta_1 - q_2) + V_{10z}Sq_3]^2 \\ &\quad + [V_{8z} - V_{9z}C(\beta_1 - q_2) + V_{10z}Cq_3 + V_{9x}S(\beta_1 - q_2) - V_{10x}Sq_3]^2 \end{aligned} \quad (2.88)$$

Organizing the right hand side terms:

$$A_6 = V_{8x} - V_{9x}C(\beta_1 - q_2) + V_{10x}Cq_3 - V_{9z}S(\beta_1 - q_2) + V_{10z}Sq_3 \quad (2.89)$$

$$B_6 = V_{8z} - V_{9z}C(\beta_1 - q_2) + V_{10z}Cq_3 + V_{9x}S(\beta_1 - q_2) - V_{10x}Sq_3 \quad (2.90)$$

The partial derivative of (2.88) with respect to q_3 is:

$$D_6 = A_6(-V_{10x}Sq_3 + V_{10z}Cq_3) + B_6(-V_{10z}Sq_3 - V_{10x}Cq_3) \quad (2.91)$$

The partial derivative of (2.88) with respect to β_1 is:

$$E_6 = A_6(V_{9x}S(\beta_1 - q_2) - V_{9z}C(\beta_1 - q_2)) + B_6(V_{9z}S(\beta_1 - q_2) + V_{9x}C(\beta_1 - q_2)) \quad (2.92)$$

The partial derivative of (2.88) with respect to q_2 is:

$$F_6 = A_6(-V_{9x}S(\beta_1 - q_2) + V_{9z}C(\beta_1 - q_2)) + B_6(-V_{9z}S(\beta_1 - q_2) - V_{9x}C(\beta_1 - q_2)) \quad (2.93)$$

The relationship between q_3 and M_i for $i = 1, 2, 3$ is:

$$0 = D_6 \frac{\partial q_3}{\partial M_i} + E_6 \frac{\partial \beta_1}{\partial M_i} + F_6 \frac{\partial q_2}{\partial M_i} \quad (2.94)$$

$\frac{\partial q_2}{\partial M_3} = 0$, which gives:

$$\frac{\partial q_3}{\partial M_1} = -\frac{E_6}{D_6} \frac{\partial \beta_1}{\partial M_1} - \frac{F_6}{D_6} \frac{\partial q_2}{\partial M_1} \quad (2.95)$$

$$\frac{\partial q_3}{\partial M_2} = -\frac{E_6}{D_6} \frac{\partial \beta_1}{\partial M_2} - \frac{F_6}{D_6} \frac{\partial q_2}{\partial M_2} \quad (2.96)$$

$$\frac{\partial q_3}{\partial M_3} = -\frac{E_6}{D_6} \frac{\partial \beta_1}{\partial M_3} \quad (2.97)$$

2.4.7 Velocity relation between q_4 and M_2, M_2, M_3, M_4

Using the sixth and final loop-closure equation (2.16), we denote $I\vec{J}$ as \mathbf{V}_{11} , $I\vec{H}$ as \mathbf{V}_{12} and $J\vec{K}$ as \mathbf{V}_{13} . Setting the magnitudes of the vectors and scalar equal we get:

$$\begin{aligned} l_7^2 &= [V_{11x}C(q_2 + q_3) - V_{12x}C\beta_3 + V_{13x}C(q_2 + q_3 + q_4) \\ &\quad + V_{11z}S(q_2 + q_3) - V_{12z}S\beta_3 + V_{13z}S(q_2 + q_3 + q_4)]^2 \\ &\quad + [V_{11z}C(q_2 + q_3) - V_{12z}C\beta_3 + V_{13z}C(q_2 + q_3 + q_4) \\ &\quad - V_{11x}S(q_2 + q_3) + V_{12x}S\beta_3 - V_{13x}S(q_2 + q_3 + q_4)]^2 \end{aligned} \quad (2.98)$$

Organizing the right hand side terms:

$$\begin{aligned} A_7 &= V_{11x}C(q_2 + q_3) - V_{12x}C\beta_3 + V_{13x}C(q_2 + q_3 + q_4) \\ &\quad + V_{11z}S(q_2 + q_3) - V_{12z}S\beta_3 + V_{13z}S(q_2 + q_3 + q_4) \end{aligned} \quad (2.99)$$

$$\begin{aligned} B_7 &= V_{11z}C(q_2 + q_3) - V_{12z}C\beta_3 + V_{13z}C(q_2 + q_3 + q_4) \\ &\quad - V_{11x}S(q_2 + q_3) + V_{12x}S\beta_3 - V_{13x}S(q_2 + q_3 + q_4) \end{aligned} \quad (2.100)$$

The partial derivative of (2.98) with respect to q_4 is:

$$\begin{aligned} D_7 &= A_7(-V_{13x}S(q_2 + q_3 + q_4) + V_{13z}C(q_2 + q_3 + q_4)) \\ &\quad + B_7(-V_{13z}S(q_2 + q_3 + q_4) - V_{13x}C(q_2 + q_3 + q_4)) \end{aligned} \quad (2.101)$$

The partial derivative of (2.98) with respect to q_3 is:

$$\begin{aligned} E_7 = & A_7(-V_{11x}S(q_2 + q_3) - V_{13x}S(q_2 + q_3 + q_4) + V_{11z}C(q_2 + q_3) + V_{13z}C(q_2 + q_3 + q_4)) \\ & + B_7(-V_{11z}S(q_2 + q_3) - V_{13z}S(q_2 + q_3 + q_4) - V_{11x}C(q_2 + q_3) - V_{13x}C(q_2 + q_3 + q_4)) \end{aligned} \quad (2.102)$$

The partial derivative of (2.98) with respect to q_2 is the same as the partial derivative with respect to q_3 . The partial derivative of (2.98) with respect to β_3 is:

$$F_7 = A_7(V_{12x}S\beta_3 - V_{12z}C\beta_3) + B_7(V_{12z}S\beta_3 + V_{12x}C\beta_3) \quad (2.103)$$

The relationship between q_4 and M_i for $i = 1, 2, 3, 4$ is:

$$0 = D_7 \frac{\partial q_4}{\partial M_i} + E_7 \frac{\partial q_3}{\partial M_i} + E_7 \frac{\partial q_2}{\partial M_i} + F_7 \frac{\partial \beta_3}{\partial M_i} \quad (2.104)$$

$\frac{\partial q_2}{\partial M_3} = \frac{\partial q_2}{\partial M_4} = \frac{\partial q_3}{\partial M_4} = \frac{\partial \beta_3}{\partial M_3} = 0$, which gives:

$$\frac{\partial q_4}{\partial M_1} = -\frac{E_7}{D_7} \frac{\partial q_3}{\partial M_1} - \frac{E_7}{D_7} \frac{\partial q_2}{\partial M_1} - \frac{F_7}{D_7} \frac{\partial \beta_3}{\partial M_1} \quad (2.105)$$

$$\frac{\partial q_4}{\partial M_2} = -\frac{E_7}{D_7} \frac{\partial q_3}{\partial M_2} - \frac{E_7}{D_7} \frac{\partial q_2}{\partial M_2} - \frac{F_7}{D_7} \frac{\partial \beta_3}{\partial M_2} \quad (2.106)$$

$$\frac{\partial q_4}{\partial M_3} = -\frac{E_7}{D_7} \frac{\partial q_3}{\partial M_3} \quad (2.107)$$

$$\frac{\partial q_4}{\partial M_4} = -\frac{F_7}{D_7} \frac{\partial \beta_3}{\partial M_4} \quad (2.108)$$

2.4.8 Constructing the Jacobian

As previously discussed, the Jacobian cannot be constructed in the standard manner, as we do not have direct control over the joints. The standard Jacobian is represented with:

$$\mathbf{J} = \begin{bmatrix} J_v \\ J_\omega \end{bmatrix} \quad (2.109)$$

where J_v and J_ω are the linear and angular velocity components of the Jacobian, respectively. These can be constructed separately, then compiled together. First, let's look at the linear velocity Jacobian. Typically, each column would be represented by $[\frac{\partial x}{\partial q_i}, \frac{\partial y}{\partial q_i}, \frac{\partial z}{\partial q_i}]^T$, however, we are controlling the motors, so we need $[\frac{\partial x}{\partial M_i}, \frac{\partial y}{\partial M_i}, \frac{\partial z}{\partial M_i}]^T$ for $i = 1, 2, 3, 4$. This can be done by extracting the first three rows from the last column of $\frac{\partial T_{\mathcal{O}}^{J_{EE}}}{\partial M_i}$, where:

$$\frac{\partial T_{\mathcal{O}}^{J_{EE}}}{\partial M_i} = \sum_{j=1}^4 \frac{\partial T_{\mathcal{O}}^{J_{EE}}}{\partial q_j} \frac{\partial q_j}{\partial M_i} \quad (2.110)$$

for $i = 1, 2, 3, 4$. $\frac{\partial q_j}{\partial M_i}$ for all i and j have been defined, so we just need to find $\frac{\partial T_{\mathcal{O}}^{J_{EE}}}{\partial q_j}$.

$$\frac{\partial T_{\mathcal{O}}^{J_1}}{\partial q_1} = \begin{bmatrix} -S q_1 & 0 & C q_1 & 0 \\ 0 & 0 & 0 & 0 \\ -C q_1 & 0 & -S q_1 & 0 \\ 0 & 0 & 0 & 0 \end{bmatrix} \quad (2.111)$$

$$\frac{\partial T_{\mathcal{O}}^{J_2}}{\partial q_2} = \begin{bmatrix} 0 & 0 & 0 & 0 \\ 0 & -S q_2 & -C q_2 & 0 \\ 0 & C q_2 & -S q_2 & 0 \\ 0 & 0 & 0 & 0 \end{bmatrix} \quad (2.112)$$

$$\frac{\partial T_{\mathcal{O}}^{J_3}}{\partial q_3} = \begin{bmatrix} 0 & 0 & 0 & 0 \\ 0 & -S q_3 & -C q_3 & 0 \\ 0 & C q_3 & -S q_3 & 0 \\ 0 & 0 & 0 & 0 \end{bmatrix} \quad (2.113)$$

$$\frac{\partial T_{\mathcal{J}_3}^{\mathcal{J}_4}}{\partial q_4} = \begin{bmatrix} 0 & 0 & 0 & 0 \\ 0 & -S q_4 & -C q_4 & 0 \\ 0 & C q_4 & -S q_4 & 0 \\ 0 & 0 & 0 & 0 \end{bmatrix} \quad (2.114)$$

We can now find the partial derivatives of the homogeneous transformation matrix with respect to each motor:

$$\begin{aligned} \frac{\partial T_{\mathcal{O}}^{\mathcal{J}_{EE}}}{\partial M_1} &= \frac{\partial T_{\mathcal{O}}^{\mathcal{J}_1}}{\partial q_1} \frac{\partial q_1}{\partial M_1} T_{\mathcal{J}_1}^{\mathcal{J}_2} T_{\mathcal{J}_2}^{\mathcal{J}_3} T_{\mathcal{J}_3}^{\mathcal{J}_4} T_{\mathcal{J}_4}^{\mathcal{J}_{EE}} + T_{\mathcal{O}}^{\mathcal{J}_1} \frac{\partial T_{\mathcal{J}_1}^{\mathcal{J}_2}}{\partial q_2} \frac{\partial q_2}{\partial M_1} T_{\mathcal{J}_2}^{\mathcal{J}_3} T_{\mathcal{J}_3}^{\mathcal{J}_4} T_{\mathcal{J}_4}^{\mathcal{J}_{EE}} \\ &\quad + T_{\mathcal{O}}^{\mathcal{J}_1} T_{\mathcal{J}_1}^{\mathcal{J}_2} \frac{\partial T_{\mathcal{J}_2}^{\mathcal{J}_3}}{\partial q_3} \frac{\partial q_3}{\partial M_1} T_{\mathcal{J}_3}^{\mathcal{J}_4} T_{\mathcal{J}_4}^{\mathcal{J}_{EE}} + T_{\mathcal{O}}^{\mathcal{J}_1} T_{\mathcal{J}_1}^{\mathcal{J}_2} T_{\mathcal{J}_2}^{\mathcal{J}_3} \frac{\partial T_{\mathcal{J}_3}^{\mathcal{J}_4}}{\partial q_4} \frac{\partial q_4}{\partial M_1} T_{\mathcal{J}_4}^{\mathcal{J}_{EE}} \end{aligned} \quad (2.115)$$

$$\begin{aligned} \frac{\partial T_{\mathcal{O}}^{\mathcal{J}_{EE}}}{\partial M_2} &= T_{\mathcal{O}}^{\mathcal{J}_1} \frac{\partial T_{\mathcal{J}_1}^{\mathcal{J}_2}}{\partial q_2} \frac{\partial q_2}{\partial M_2} T_{\mathcal{J}_2}^{\mathcal{J}_3} T_{\mathcal{J}_3}^{\mathcal{J}_4} T_{\mathcal{J}_4}^{\mathcal{J}_{EE}} + T_{\mathcal{O}}^{\mathcal{J}_1} T_{\mathcal{J}_1}^{\mathcal{J}_2} \frac{\partial T_{\mathcal{J}_2}^{\mathcal{J}_3}}{\partial q_3} \frac{\partial q_3}{\partial M_2} T_{\mathcal{J}_3}^{\mathcal{J}_4} T_{\mathcal{J}_4}^{\mathcal{J}_{EE}} \\ &\quad + T_{\mathcal{O}}^{\mathcal{J}_1} T_{\mathcal{J}_1}^{\mathcal{J}_2} T_{\mathcal{J}_2}^{\mathcal{J}_3} \frac{\partial T_{\mathcal{J}_3}^{\mathcal{J}_4}}{\partial q_4} \frac{\partial q_4}{\partial M_2} T_{\mathcal{J}_4}^{\mathcal{J}_{EE}} \end{aligned} \quad (2.116)$$

$$\frac{\partial T_{\mathcal{O}}^{\mathcal{J}_{EE}}}{\partial M_3} = T_{\mathcal{O}}^{\mathcal{J}_1} T_{\mathcal{J}_1}^{\mathcal{J}_2} \frac{\partial T_{\mathcal{J}_2}^{\mathcal{J}_3}}{\partial q_3} \frac{\partial q_3}{\partial M_3} T_{\mathcal{J}_3}^{\mathcal{J}_4} T_{\mathcal{J}_4}^{\mathcal{J}_{EE}} + T_{\mathcal{O}}^{\mathcal{J}_1} T_{\mathcal{J}_1}^{\mathcal{J}_2} T_{\mathcal{J}_2}^{\mathcal{J}_3} \frac{\partial T_{\mathcal{J}_3}^{\mathcal{J}_4}}{\partial q_4} \frac{\partial q_4}{\partial M_3} T_{\mathcal{J}_4}^{\mathcal{J}_{EE}} \quad (2.117)$$

$$\frac{\partial T_{\mathcal{O}}^{\mathcal{J}_{EE}}}{\partial M_4} = T_{\mathcal{O}}^{\mathcal{J}_1} T_{\mathcal{J}_1}^{\mathcal{J}_2} T_{\mathcal{J}_2}^{\mathcal{J}_3} \frac{\partial T_{\mathcal{J}_3}^{\mathcal{J}_4}}{\partial q_4} \frac{\partial q_4}{\partial M_4} T_{\mathcal{J}_4}^{\mathcal{J}_{EE}} \quad (2.118)$$

This gives the linear velocity Jacobian:

$$J_v = \left[\frac{\partial T_{\mathcal{O}}^{\mathcal{J}_{EE}}}{\partial M_1}(1 : 3, 4) \quad \frac{\partial T_{\mathcal{O}}^{\mathcal{J}_{EE}}}{\partial M_2}(1 : 3, 4) \quad \frac{\partial T_{\mathcal{O}}^{\mathcal{J}_{EE}}}{\partial M_3}(1 : 3, 4) \quad \frac{\partial T_{\mathcal{O}}^{\mathcal{J}_{EE}}}{\partial M_4}(1 : 3, 4) \right] \quad (2.119)$$

We now examine the angular velocity Jacobian, J_ω . The columns of J_ω typically correspond to the axes of rotation of the joints, expressed in the world frame. However, once again, we must adjust the Jacobian accordingly, as we are multiplying it by motor velocities rather than joint velocities. We can do this by summing the effects each motor has on each joint, using the previously derived joint-motor relationships.

$$J_\omega = \sum_{n=1}^4 W_n = \sum_{n=1}^4 \mathbf{R}_{\mathcal{O}}^{\mathcal{J}_n} \hat{\omega}_n \begin{bmatrix} \frac{\partial q_n}{\partial M_1} & \frac{\partial q_n}{\partial M_2} & \frac{\partial q_n}{\partial M_3} & \frac{\partial q_n}{\partial M_4} \end{bmatrix} \quad (2.120)$$

where $\mathbf{R}_{\mathcal{O}}^{J_n}$ is the rotation matrix from the base frame to the frame at joint n , i.e. $\mathbf{T}_{\mathcal{O}}^{J_n}(1:3,1:3)$ and $\hat{\omega}_n$ is the axis of rotation at the n^{th} joint.

2.5 Kinematic Simulations

In this section, we will simulate the movement of the thumb using MATLAB Simulink. Using the *Transform Sensor* block in Simulink, we can generate graphs of the thumb tip's position as each trial is executed. Each trial consists of one or more segments. For each segment a start pose, end pose, and duration were specified. Using the differences between the poses and the specified time, the necessary linear and angular velocities were calculated. Using Equation 2.47, the necessary motor velocities for the given task space velocity were calculated. The motor velocity is then multiplied by the time step (0.01 seconds for all trials) and added to the current motor position. This is repeated until an acceptable error level was reached. An error of 0.25 mm in each direction and 1° for the global thumb tip angle was used for all trials. A pose is represented as $[x, y, z, \alpha]$. In order to determine a valid α for each pose, we iterate through values of α from 0° to 270°, computing the inverse kinematics at each step and returning the values of α that yield acceptable intermediate joint angles and motor positions. When analyzing the motor velocities we aim for values less than 8 mm/s, as this is the maximum linear velocity for the Faulhaber motors used in the finger; however, larger motors with faster speeds could be used instead, at the expense of a slightly larger hand. The code for these simulations, as well as the kinematics, can be found at [2]. A supplementary video showing the simulations can be found at [3].

2.5.1 Path Following

First, we demonstrate the movement of the thumb along a path in the YZ plane. The desired path consists of the following poses: $[0, 70, 70, -125^\circ]$, $[0, 100, 70, -95^\circ]$, $[0, 100, 40, -125^\circ]$, $[0, 70, 40, -165^\circ]$, $[0, 70, 70, -125^\circ]$. Each segment of the path is executed over 1.5 seconds, corresponding to a linear velocity of 15 mm/s.

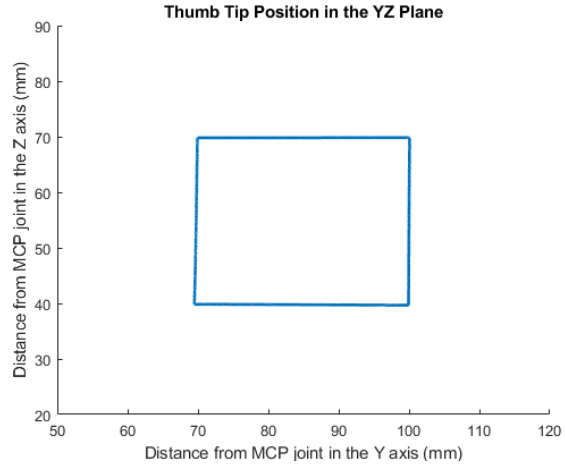


Figure 2.14: Thumb Tip Position for YZ Planar Motion

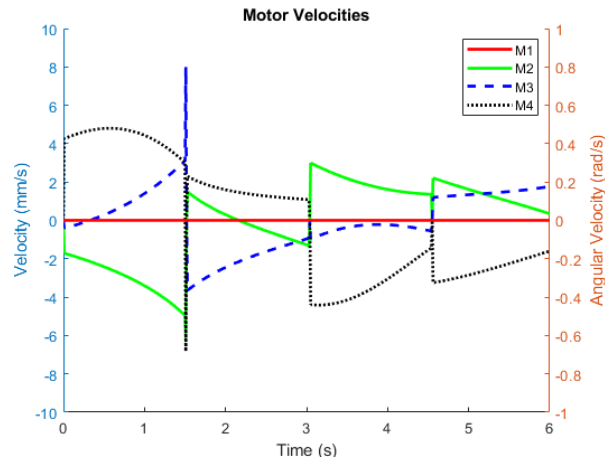


Figure 2.15: Motor Velocities for YZ Planar Motion

Next, we will examine motion in the XZ plane (abduction). The desired path consists of the following poses: $[15,90,90,-60^\circ]$, $[-15,90,90,-60^\circ]$, $[-15,90,60,-110^\circ]$, $[15,90,60,-110^\circ]$, $[15,90,90,-60^\circ]$. Once again, each segment of the path is executed over 1.5 seconds, corresponding to a linear velocity of 15 mm/s.

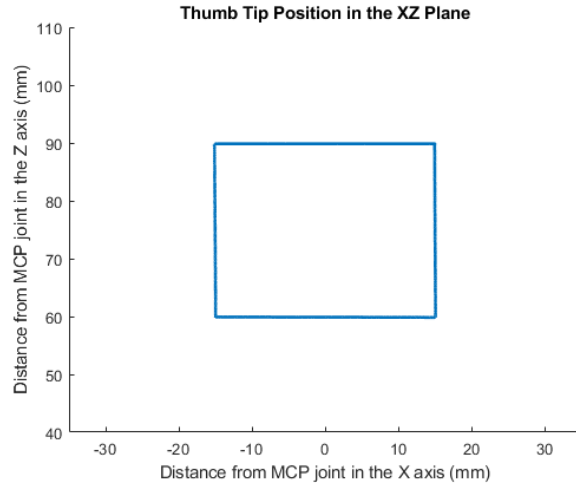


Figure 2.16: Thumb Tip Position for XZ Planar Motion

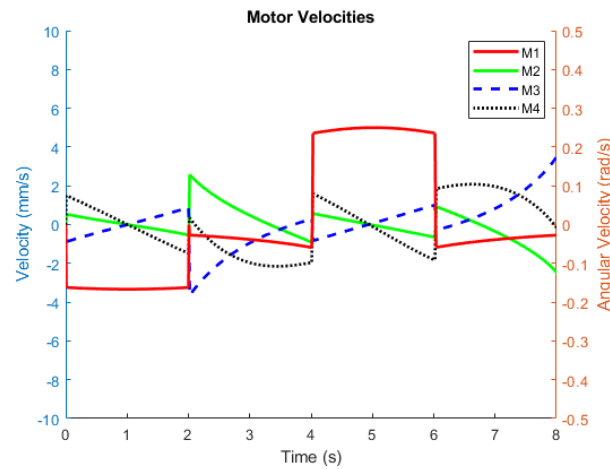


Figure 2.17: Motor Velocities for XZ Planar Motion

In both cases, the thumb tip closely follows the desired path, and the motor velocities remain within a reasonable range. Additionally, the total time to complete the path was 6 seconds, indicating that the thumb tip maintained the desired velocity throughout.

2.5.2 Sliding Contact

In this demonstration, the thumb is moved along a desired path while maintaining a constant global thumb tip angle. This type of motion is useful in scenarios where arm movement is restricted and an object must be slid within the palm or against the index finger, while preserving a consistent point of contact. The desired path for this motion is: [0,70,70,-125°], [0,80,70,-125°]. The total time for this motion is 2 seconds, corresponding to a linear velocity of 5 mm/s.

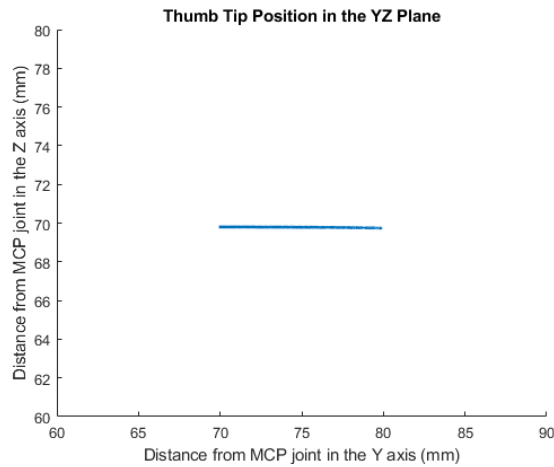


Figure 2.18: Thumb Tip Position for Sliding Motion

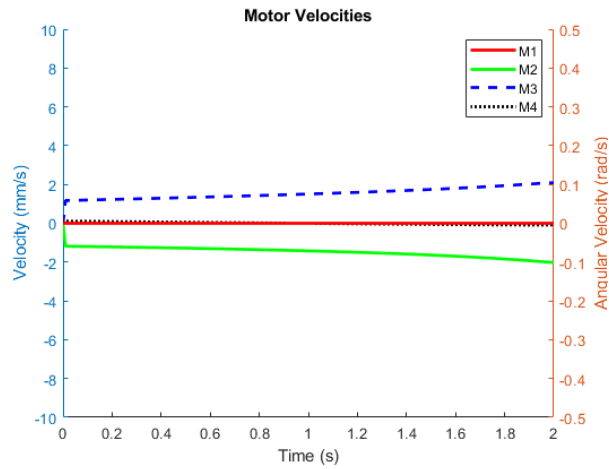


Figure 2.19: Motor Velocities for Sliding Motion

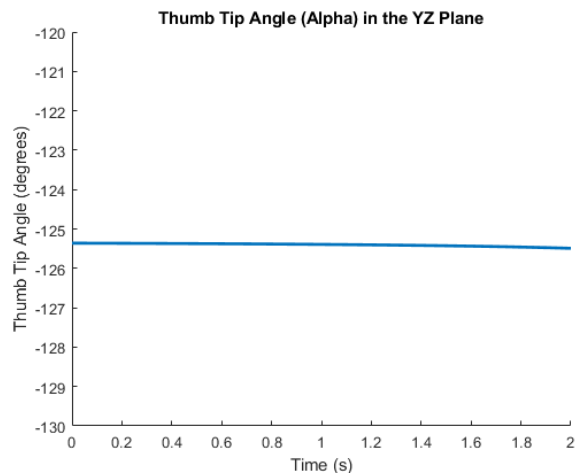


Figure 2.20: Thump Tip Angle during Sliding Motion

While there is some error in the thumb tip angle, it is well within the acceptable range of $\pm 1^\circ$, and remains there as the thumb moves smoothly from $y = 70$ mm to $y = 80$ mm.

2.5.3 Pivoting Contact

In this demonstration, the thumb remains at a fixed position while the global thumb tip angle is varied. This type of motion is useful when the arm is moving but a constant contact point on an object must be maintained. The desired path for this motion is: $[0,95,60,-95^\circ]$, $[0,95,60,-115^\circ]$. The total time for this motion is 2 seconds, corresponding to an angular velocity of 0.1745 radians per second.

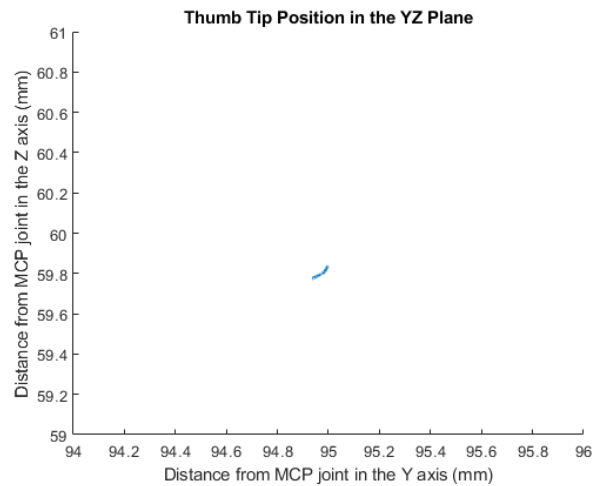


Figure 2.21: Thumb Tip Position for Pivoting Motion

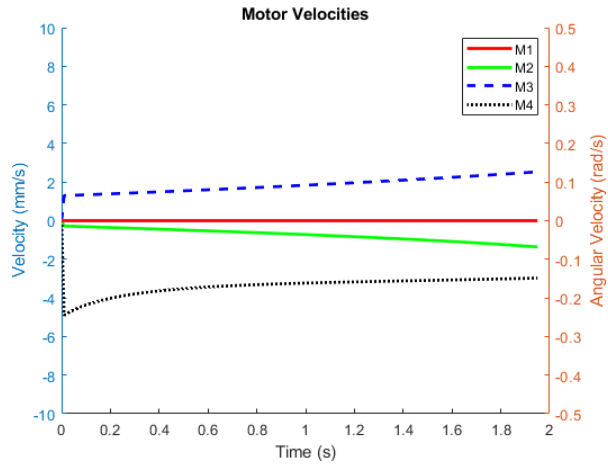


Figure 2.22: Motor Velocities for Pivoting Motion

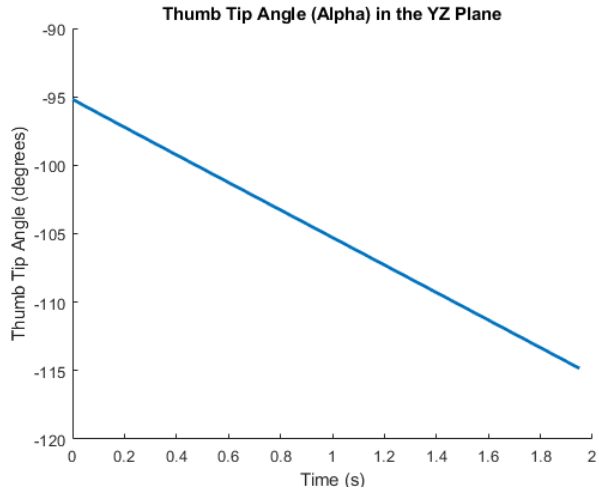


Figure 2.23: Thump Tip Angle during Pivoting Motion

This demonstration was highly successful, as the thumb tip shifted less than 0.25 mm from its initial position while rotating linearly from -95° to -125° .

In summary, this chapter has established the full kinematic characterization of a 4-DoF series-parallel thumb mechanism, including forward, inverse, and differential kinematics. An additional rotational degree of freedom was

incorporated and the abduction range extended, enabling precise control of the thumbtip’s position in task space. This added degree of freedom also facilitates orientation control—capability that the 3-DoF configuration lacks. Simulation results confirm the feasibility of the derived kinematics for executing thumb trajectories relevant to dexterous manipulation, thereby validating the design’s ability to meet the pose requirements outlined in Chapter 1.

Chapter 3

Detailed Design of the 3-DoF Finger

Before considering the thumb's place in a hand, we must first construct a detailed design of the finger. This will provide a more accurate representation of the size of the finger, as well as its reachable workspace. First, we must lay out some design goals.

1. **Ease of Manufacturing** Like most prototypes our goal will be to 3D print as many parts as possible, but we may defer to machined aluminum parts if extra strength is needed. The motors must also be easily replaceable in case of failure.
2. **Cost** High quality robotic hands are not a cheap endeavor. Retail costs range from \$3,000-\$24,000 [46] [17] per finger. The LEAP hand introduces the most affordable option at approximately \$2,000, though you must construct the hand yourself [45]. Additionally, it has no sensing capabilities, and has large fingers as it is direct drive. Our budget is \$2,500, though this is a flexible number, as Dr. Chakraborty has expressed that purchasing parts from reputable vendors takes priority over minimizing cost.
3. **Size** Our goal is to maintain a size similar to that of the existing linkage driven finger (20 mm x 100 mm x 22 mm) and palm thickness (25 mm x 120 mm x 89.5 mm)
4. **Shape and Sensing** We do not consider the outer shape of the phalanges, or the finger's sensing capabilities. These problems must be

addressed in the future.

5. **Range of Motion** We must ensure that the MCP abduction range is at least $\pm 20^\circ$, and the MCP, PIP, and DIP flexion range is 0° – 90° .
6. **Controllability** Lastly, we must ensure that each joint can be actuated in 1° increments based on the resolution of the motor encoder.

3.1 Finger Structure

The finger will be based on the kinematic structure outlined in [51]. The only modification is that the first loop will be replaced by a direct-drive motor. Because the joint is located close to the palm, it is much simpler to actuate it with a direct-drive motor. Figure 3.1 shows the naming convention for the linkages. P_2 and P_3 represent the vector from the MCP joint to M_2 and M_3 when M_2 and M_3 equal 0. Note that l and P start indexing at 2. This is because they are used in conjunction with motors 2 and 3. Since M_1 is direct-drive, l_1 and P_1 do not exist.

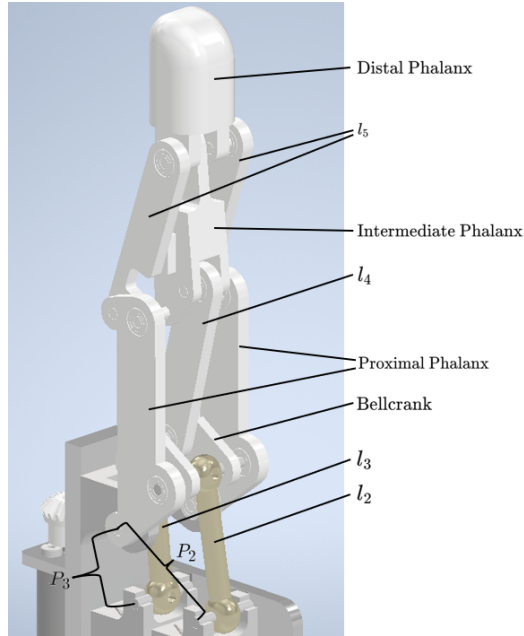


Figure 3.1: Finger Link Diagram

Figure 3.2 shows the naming convention that will be used in this paper to refer to each joint.

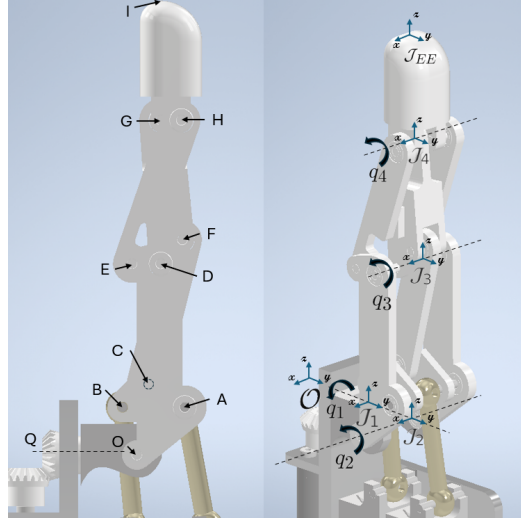


Figure 3.2: Finger Joint Diagram

As in the previous section, alphabetic notation is used to describe vectors, particularly in the context of linkage design. i.e., \vec{OA} would describe the vector on the proximal phalanx, from joint O to joint A. When describing the finger as a serial manipulator, \mathcal{J}_n will be used to describe the reference frames at each serial joint. \mathcal{O} represents the origin (world frame), while \mathcal{J}_{EE} represents the end-effector frame. Although \mathcal{O} , \mathcal{J}_1 , and \mathcal{J}_2 coincide spatially, they have been separated in Figure 3.2 for clarity.

3.2 Minimum Dimensions and Hardware Selection

Determining the minimum size of the linkages first requires selecting the bearings and pins. We will be using the 52-2Z bearings, as they are the smallest metric bearings available from McMaster-Carr [39]. They have an inner diameter of 2 mm, an outer diameter of 5 mm, and a thickness of 2.5 mm. Accordingly, each link must be 2.5 mm thick. This also means we will need 2 mm diameter pins (steel, McMaster-Carr). Assuming 2 mm of

material between outer diameters, we get the following minimum distances for each linkage:

1. $\vec{AB}, \vec{AC}, \vec{BC}, \vec{GH}, \vec{KM} \geq 4 \text{ mm}$
2. $\vec{AO}, \vec{AE}, \vec{EF}, l_4, l_5, \vec{GI}, \vec{HI} \geq 5.5 \text{ mm}$

The smallest rod-ends available are the Cockrill Micro Nickle Rod Ends [16], which have a length of 12.62 mm (from one end to the center of the ball joint). This means that l_2 and l_3 must be longer than 25.24 mm. The linear actuators selected to move $\mathbf{M}_{2,3}$ were the Faulhaber 08L-SL16:1. These motors were selected due to their superior size to torque ratio as compared to the MAXON motors used by the ILDA hand group [31] [38] [24]. Additionally, they have the option to interface the lead screw directly into the motor. This eliminates the need to use a collar to attach the lead screw to the motor. The maximum radial force the lead screw can withstand is only 5 N. This means the lead screw must be supported by a linear guide rail. The ICO LWLC3 rails were used, once again for their size [27]. A custom carriage was designed to interface the lead screw nut to the rail car. It is a 3-D printed component with threaded inserts to connect it to the nut and car. Allowing 1 mm of clearance between the outside of the ball joint of \mathbf{M}_3 and the carriage of \mathbf{M}_2 gives a minimum distance of 15 mm between the axes of \mathbf{M}_2 and \mathbf{M}_3 . This adds another size constraint:

3. $P_{2y} - P_{3y} \geq 15 \text{ mm}$

The abduction motor is the Faulhaber 1226A012B-16:1 brushless DC motor. A larger motor was chosen for \mathbf{M}_1 since it is direct drive and would not gain the mechanical advantage of the lead screw. Additionally, this motor comes with mounting holes, making it easier to incorporate into the assembly. Figure 3.4 shows the miter gears (plastic, McMaster-Carr) used to translate the motion, as well as the \mathbf{M}_2 screws used to secure the motor. The smaller motors have no such mounting holes and must be clamped in place. Figure 3.5 shows the clamp piece, secured by 0-80 screws, washers, and nuts (McMaster-Carr). So, should \mathbf{M}_2 or \mathbf{M}_3 fail, the clamp can easily be removed, and the lead screw nut can be unthreaded from the carriage.

Finally, we need to know the minimum distance the motor can move the nut. The motor is equipped with a 1024 increment encoder, giving a resolution of 0.35° . However, these small motors rotate extremely fast ($n_o = 37500 \text{ rpm}$). Assuming a conservative control scheme with quarter-rotation

accuracy, a 16:1 reduction gearbox, and a lead screw pitch of 0.5 mm, we achieve a theoretical positioning resolution of 0.0039 mm.

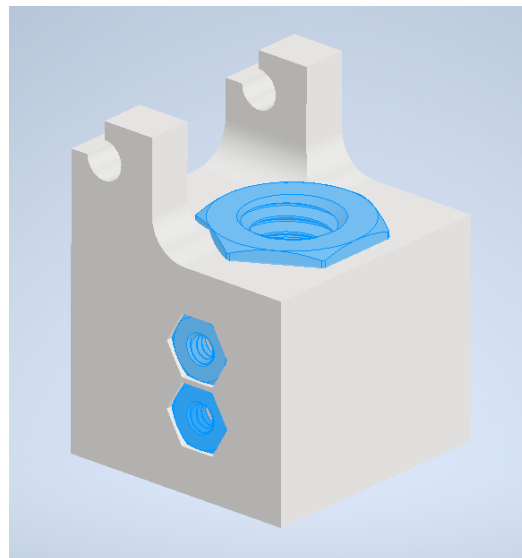


Figure 3.3: Custom Carriage (threaded inserts in blue)

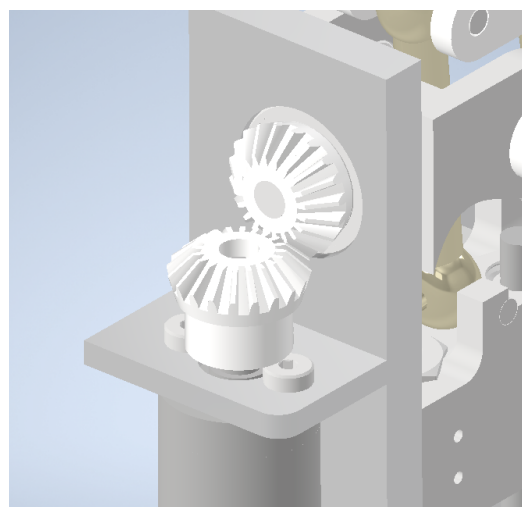


Figure 3.4: M₁ Miter Gears and Mounting System

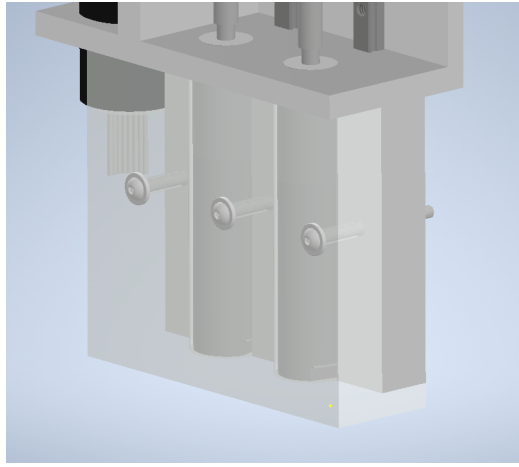


Figure 3.5: M_2 and M_3 Motor Clamp

3.3 Determining Link Dimensions

Having established the design criteria, we can now determine the dimensions of the links. This was carried out as an iterative process, beginning with the link dimensions used in [51], and modified according to the minimum size constraints. The general algorithm was as follows:

1. Change desired link lengths.
2. Adjust other links in the loop to satisfy the loop-closure equations.
3. Iterate through the joint space (one-degree increments), recording the corresponding motor values.
4. Verify that all values in the list are real.
5. Check the maximum and minimum values of M_2 and M_3 for a similar range of motor values (i.e. if $M_2 = [-5, 20]$ and $M_3 [5, 35]$, the usable rail section must be at least 40 mm long).
6. Check the minimum necessary change in motor position is greater than 0.0039 mm.
7. Check the maximum necessary change in motor position is less than 0.5 mm.

After numerous iterations the following link lengths were selected:

$$l_2 = l_3 = 25.24 \text{ mm}$$

$$l_4 = 30.92 \text{ mm}$$

$$l_5 = 31.72 \text{ mm}$$

$$\vec{OA} = \begin{bmatrix} 0 & 10 & 10 \end{bmatrix}^T$$

$$\vec{P}_2 = \begin{bmatrix} 0 & 14.5 & -14.836 \end{bmatrix}^T$$

$$\vec{P}_3 = \begin{bmatrix} 0 & -0.5 & -15.111 \end{bmatrix}^T$$

$$\vec{OE} = \begin{bmatrix} 0 & 5 & 40 \end{bmatrix}^T$$

$$\vec{AB} = \begin{bmatrix} 0 & -13 & 0 \end{bmatrix}^T$$

$$\vec{AC} = \begin{bmatrix} 0 & -8 & 5 \end{bmatrix}^T$$

$$\vec{GH} = \begin{bmatrix} 0 & 4.5 & 5 \end{bmatrix}^T$$

$$\vec{GI} = \begin{bmatrix} 0 & 0 & 30 \end{bmatrix}^T$$

$$\vec{KM} = \begin{bmatrix} 0 & 4.3 & 0 \end{bmatrix}^T$$

$$\vec{KT} = \begin{bmatrix} 0 & 0 & 25 \end{bmatrix}^T$$

Note that \vec{KT} can be set arbitrarily; 25 mm was chosen so the overall length is 95 mm.

3.3.1 Abduction/Adduction Angle

Besides the kinematic loops being satisfied, there are other concerns that must be addressed with respect to the adduction/abduction of the mechanism, specifically the deflection angle of the rod ends and physical collisions within the mechanism. First, the selected rod ends have maximum deflection angles of $\pm 50^\circ$, as per their datasheet. Second, we must check the CAD model for collisions. Figure 3.6 shows a collision between the rod ends and the bell crank, which occurs when the finger abducts. The only way to avoid this collision is to widen the bellcrank. This, in turn, widens the entire finger as the abductor piece, as well as the proximal links, must also be moved outwards. For the narrowest configuration, which is 23 mm wide, we can achieve 25° of abduction. This is a simple trade-off that we will have to consider more after the workspace analysis.

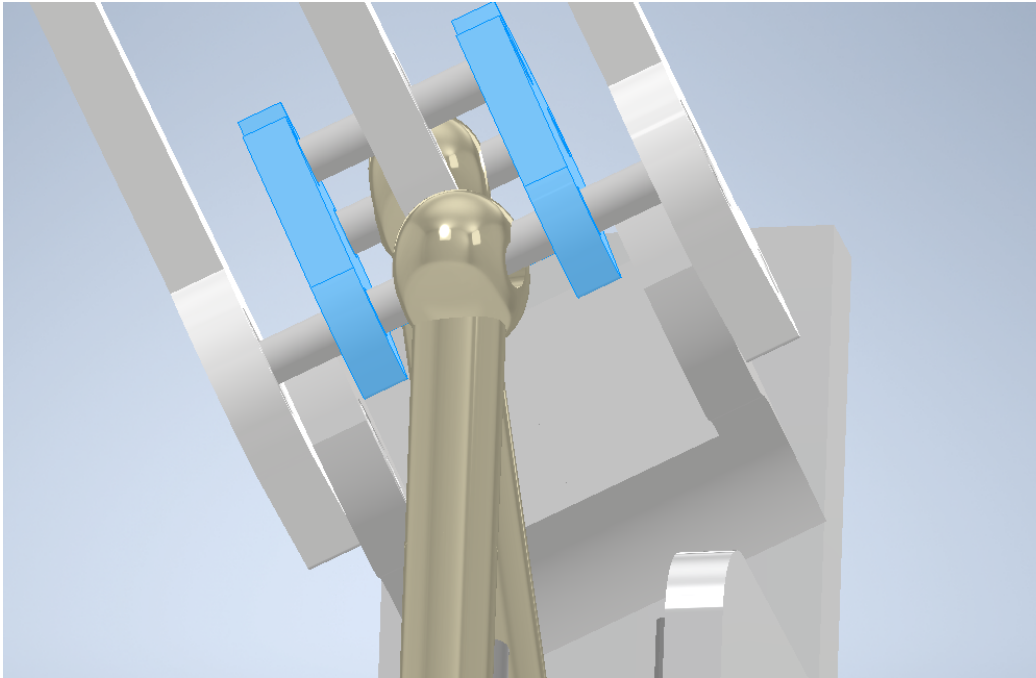


Figure 3.6: Bellcrank (blue) Colliding with a Rod End at $q_1 = 25^\circ$

It appears that there is also a collision at the spherical joint, but this is simply a visual error in Inventor. The range of deflection is well within the manufacturer's specifications.

3.4 Final Costing and Size

The final dimensions of the finger (following the format in Table 1.1) are 23(14) mm × 95 mm × 20 mm, while the motor housing (palm) measures 21.5 mm × 94.7 mm × 49.5 mm. The total mass of the assembled finger, including motor controllers, is approximately 102 grams. The cost of a single finger amounts to \$2,527.28, with a detailed cost breakdown provided in Table 3.1. Although many hardware components were only available in bulk quantities (e.g., packs of 25 or 50), their full purchase price was included in the estimate. In the end, we successfully developed a fully 3D-printed, modular finger design featuring easily removable motors, sufficient controllability, and the required range of motion—while exceeding our target budget by only 1%. Moreover, the same design methodology is directly applicable to the 4-DoF thumb, as illustrated in Figure 3.8.

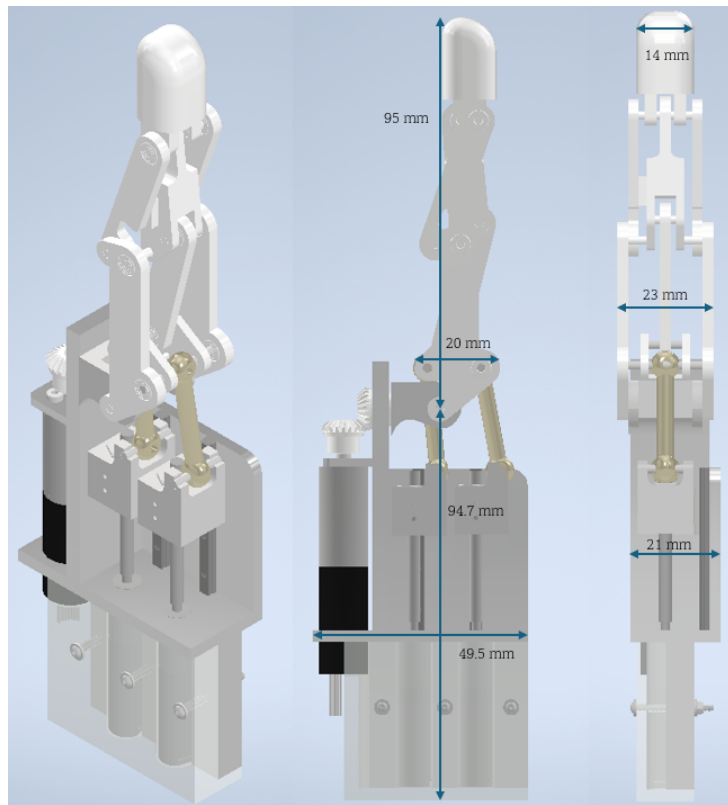


Figure 3.7: Detailed Design of 3-DoF Finger

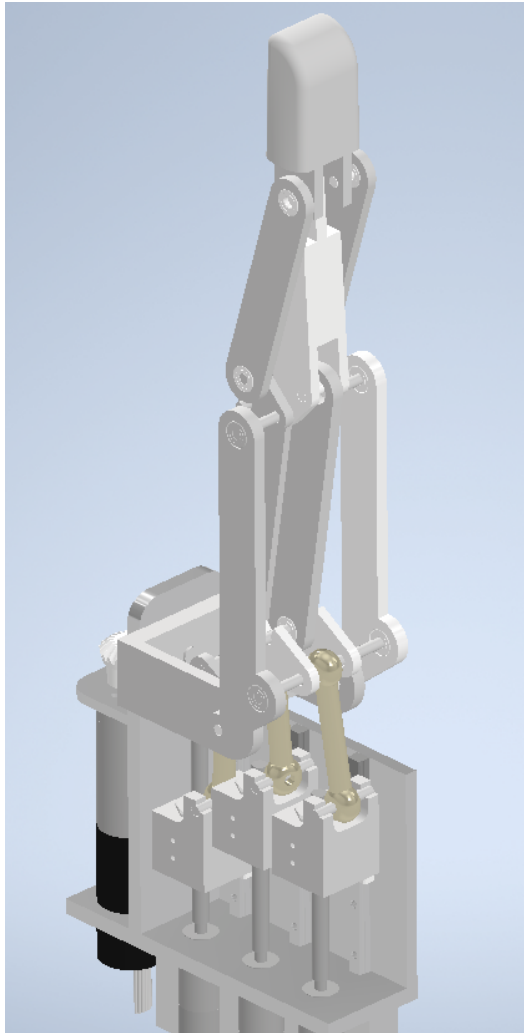


Figure 3.8: Preliminary Design of 4-DoF Thumb

Table 3.1: Bill of Materials for 3-DoF Finger

Item	Qty	Cost (\$)	Total (\$)	Supplier
2 mm Bearings	13	7.03	91.39	McMaster-Carr
8 mm Bearing	1	3.80	3.80	McMaster-Carr
Rod Ends	4	17.35	69.40	Cockrill Corp
M3 Threaded Rod	1	12.84	12.84	McMaster-Carr
M2 Pin	7	9.85	68.95	McMaster-Carr
Linear Guide Rail	2	144.70	289.40	Motion
Miter Gear	2	3.57	7.14	McMaster-Carr
0-80 Screw	1	8.56	8.56	McMaster-Carr
0-80 Washer	1	2.45	2.45	McMaster-Carr
0-80 Lock Nut	1	12.52	12.52	McMaster-Carr
M2 Machine Screw	1	12.19	12.19	McMaster-Carr
M3 Pin	1	16.44	16.44	McMaster-Carr
Flexion Motors	2	408.50	817.00	Faulhaber
Abduction Motor	1	260.00	260.00	Faulhaber
Motor Controllers	3	280.70	842.10	Faulhaber
Filament (200 g)	0.2	14.00	2.80	Amazon
Total			2,516.98	

Chapter 4

Primitive Hand Design

As previously discussed, the same components and design methodology outlined in Chapter 3 can be applied to develop a detailed model of the thumb. However, unlike the finger, the link lengths for the thumb cannot be selected arbitrarily. Instead, they must be carefully determined by analyzing the combined workspaces of the thumb and fingers. This ensures sufficient overlap between the two, enabling a broad range of pinch and grasp configurations.

4.1 Generating the Workspaces

Typically, the workspace of a serial manipulator would be mapped by discretizing the joint ranges, then iterating through each joint range using the forward kinematics to plot the end-effector location. However, this can be computationally intensive given a high joint resolution and number of joints. Additionally, having so many points plotted in MATLAB's 3-D viewer can significantly slow down the program, making it difficult to manipulate and inspect. To solve this issue, we will simply plot the boundary of the workspace. This is done by fixing certain joint angles, then iterating through the remaining joints. For example, by setting $q_1 = 25^\circ$ and iterating through $q_2 = [0^\circ, -90^\circ]$ and $q_3 = [0^\circ, -90^\circ]$ (and $q_4 = [0^\circ, -90^\circ]$ for the thumb), we can generate the sides of the workspace. We will start with the thumb phalanges being equal in length to those of the fingers. As stated in Chapter 2, the thumb has significantly more abduction than the finger, so its abduction range will be $\pm 40^\circ$. As stated in Chapter 3, we can achieve this by widening the finger. Figures 4.1 and 4.2 show the workspaces of a finger and thumb using

0.5° increments for the joint discretization.

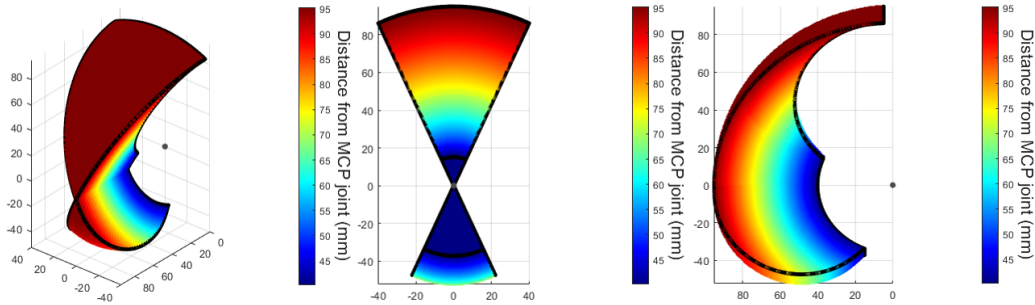


Figure 4.1: Workspace of the 3-DoF Finger

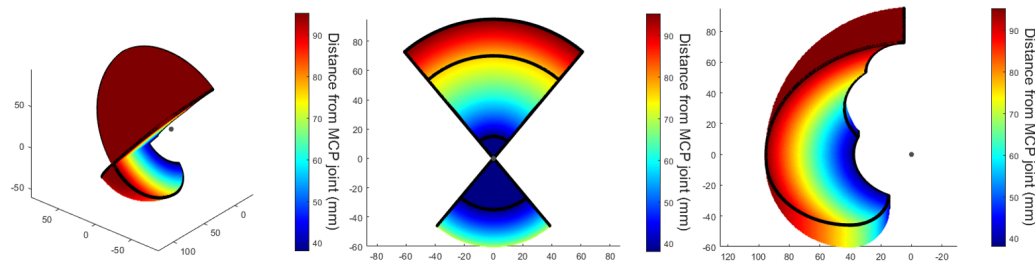


Figure 4.2: Workspace of the 4-DoF Thumb

4.2 Satisfying the Design Goals

In this section, we aim to satisfy the goals laid out in Chapter 1:

1. The index and middle fingers should be able to perform a side pinch and a top pinch.
2. The thumb should have multiple pinch positions with the index finger.
3. The thumb should be able to perform a pinch with each finger.
4. The hand should have an open palm configuration.

Since each workspace is a list of points, we can use a transformation matrix to translate and rotate the workspaces to represent multiple fingers in the same workspace. The world frame for the hand will be located at the index finger's MCP joint. The base of the finger is 21.5 mm wide. Assuming some room for mounting hardware, we will space the fingers 30 mm apart. Figure 4.3 shows the workspace of the two fingers, which has ample overlap for both a side and top pinch.

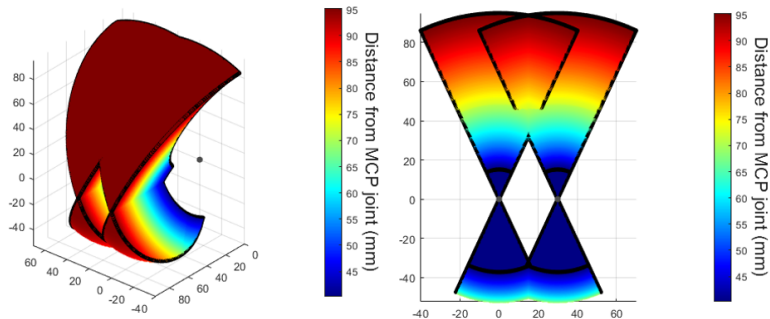


Figure 4.3: Workspace of Two Fingers Spaced 30 mm Apart

However, we must also check Simulink for collisions, which unfortunately occur (Figure 4.4).

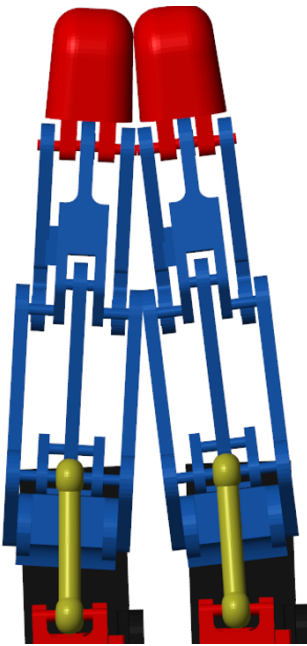


Figure 4.4: Side Pinch Simulation, Fingers Spaced 30 mm Apart

Spacing the fingers an extra 2 mm apart maintains solid workspace overlap (Figure 4.6), while eliminating the collisions in the proximal phalanges (Figure 4.6). Figure 4.7 shows the top pinch is also collision free in the 32 mm configuration, fully satisfying Condition 1.

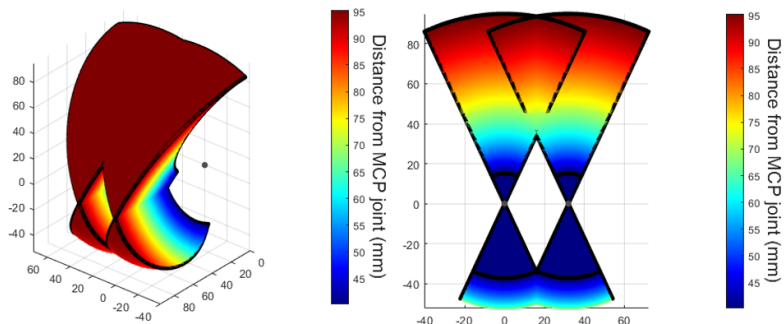


Figure 4.5: Workspace of Two Fingers Spaced 32 mm Apart

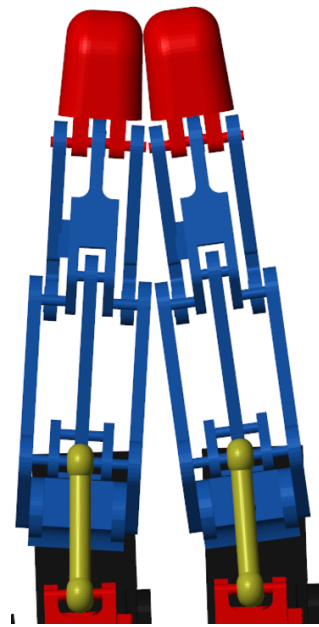


Figure 4.6: Side Pinch Simulation, Fingers Spaced 32 mm Apart

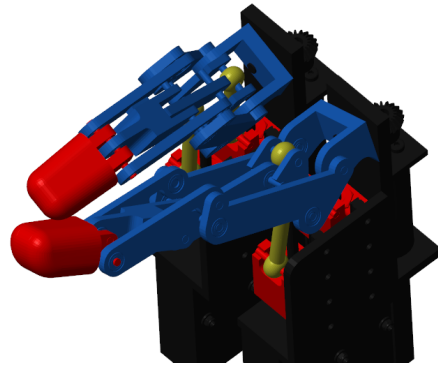


Figure 4.7: Top Pinch of Two Fingers Spaced 32 mm Apart

The extra DoF introduced to the thumb should satisfy condition 2, as long as there is ample overlap between the thumb and index finger workspaces. Conditions 4 and 3 also rely on the placement of the thumb, so these issues must be solved simultaneously. We will begin by positioning the ring finger 30 mm to the left of the middle finger (along the positive x-axis), and the pinkie

finger an additional 30 mm to the left of the ring finger. Referring back to Figure 2.1, we can see that the CMC joint of the thumb is positioned almost directly beneath the MCP joint of the index finger. This illustrates a key challenge of the series-parallel hybrid finger design: placing the motors within the palm restricts the available space for the thumb. To address this, we will position the thumb 20 mm to the right of the index finger (along the negative x-axis) and 120 mm downward (along the negative z-axis). Additionally, it will be rotated first about its x-axis, then its z-axis, with an initial rotation of 50° in each direction. Figure 4.8 shows the workspace of the fingers and thumb in this initial position.

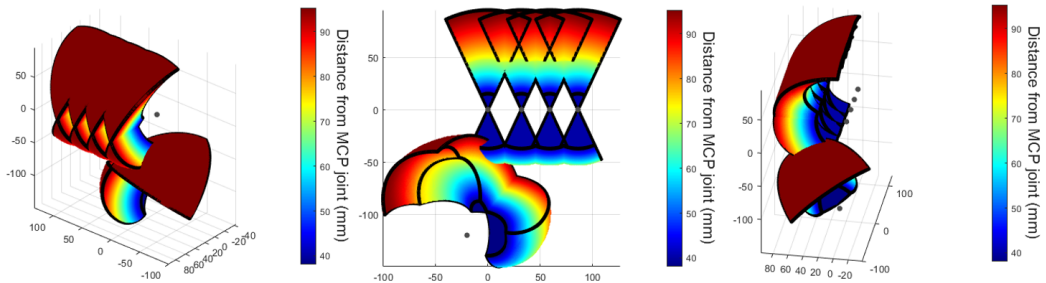


Figure 4.8: Initial Hand Workspace

Clearly, some modifications are necessary, as there is no overlap between the thumb and the non-index fingers. This was a highly iterative process that involved changes to the thumb's dimensions, the thumb's pose, as well as the finger poses. Each change was made to ensure ample workspace overlap while avoiding unwanted collisions during the pinching tasks. The key changes are as follows:

1. The thumb link lengths were increased to $d_1 = 60$ mm, $d_2 = 45$ mm, and $d_3 = 30$ mm, the y-axis rotation was increased to 70°, the x-axis rotation was increased to 55° and it was moved forward 5.5 mm.
2. The ring finger was moved down 5 mm, right 3 mm, and rotated 5° about its y-axis.
3. The pinkie finger was moved down 10 mm, right 6 mm, and rotated 10° about its y-axis.

This yields the workspace shown in Figure 4.9.

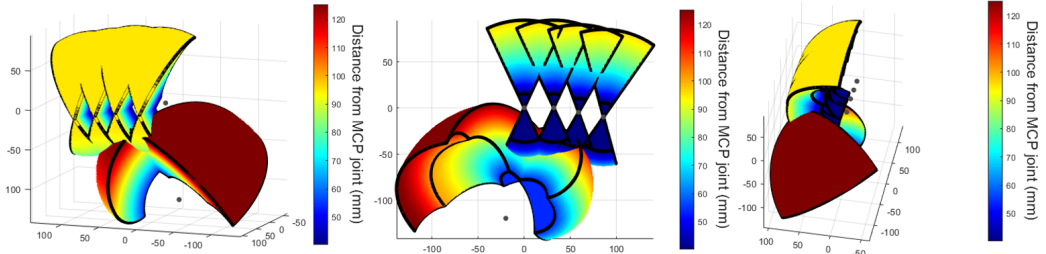


Figure 4.9: Final Hand Workspace

4.3 Hand Simulations

While we have demonstrated precise control of the thumb using task-space control, we will use simple joint-space control to demonstrate that the hand design satisfies all of our design requirements. The pinch poses were chosen by trial and error, as the purpose of this paper is to demonstrate the kinematic capability of the hand, not to devise grasping/pinching algorithms. First, the index and middle fingers perform a side pinch, followed by a top pinch. From there, the thumb forms a pinch with every finger, including an additional side pinch with the index finger. Once again the video demonstration can be found at [3]. Below are the motor velocities for each finger from the demonstration.

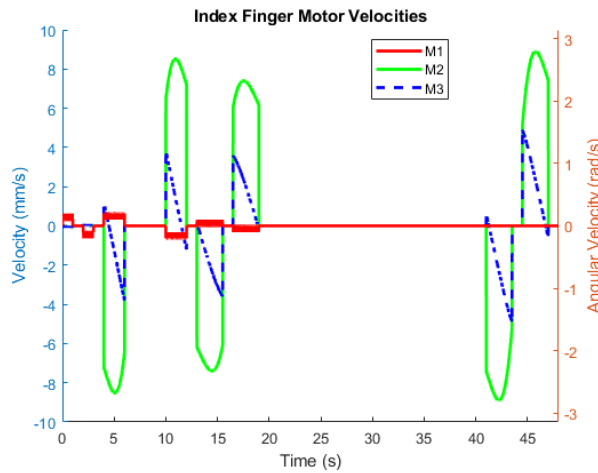


Figure 4.10: Index Finger Motor Velocities during Hand Demonstration

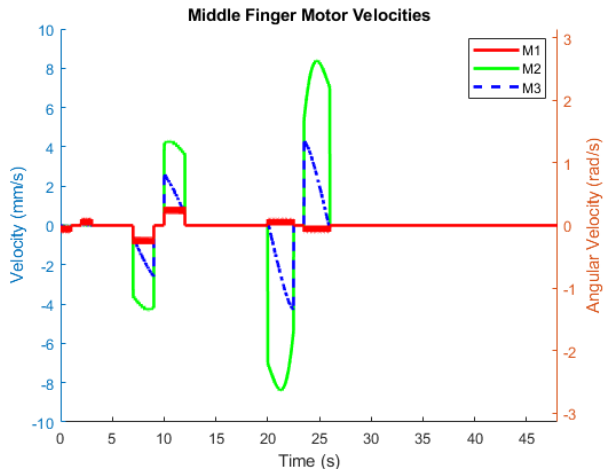


Figure 4.11: Middle Finger Motor Velocities during Hand Demonstration

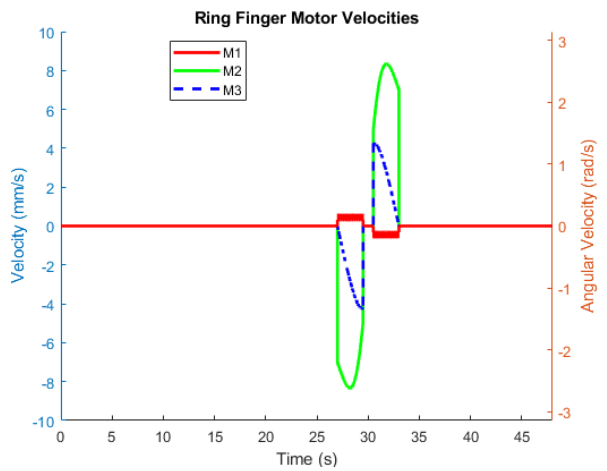


Figure 4.12: Ring Finger Motor Velocities during Hand Demonstration

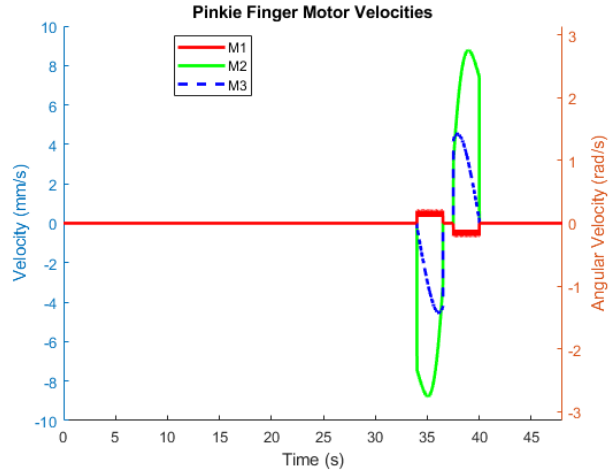


Figure 4.13: Index Finger Motor Velocities during Hand Demonstration

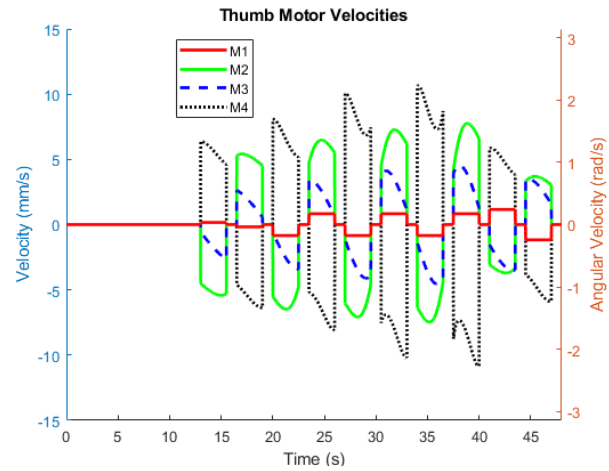


Figure 4.14: Thumb Motor Velocities during Hand Demonstration

These velocities are useful in evaluating how quickly the hand will be able to grasp objects. In this demonstration, we can see that during the thumb-to-finger pinches ($t = 2.5$ seconds), motors in both the fingers and thumb exceeded the 8 mm/s limit. Increasing the time limit to 3 seconds, yields maximum finger motor velocities of 8.6 mm/s, and maximum thumb motor velocities of 8.9 mm/s, which is still too high. Further increasing the

grasp time to 3.5 seconds gives maximum finger velocities of 7.2 mm/s and maximum thumb velocities 7.6 mm/s.

Despite its limited actuation speed, the preliminary hand design was able to successfully perform all of the required poses. A comparison of overall dimensions with existing hands is not particularly meaningful at this stage, as the final housing is expected to significantly alter the external geometry.

Chapter 5

Conclusions

While there were no unwanted collisions between the models during the shown simulations, it should be noted that in this configuration, some collisions do occur between the thumb's metacarpal linkage and the index finger's motor housing. This happens when the thumb is near maximum flexion in the CMC joint and/or near maximum abduction. Moving the thumb farther away from the fingers and increasing its link lengths is an easy fix, but it will result in worse force transmission. Otherwise, avoiding this collision would only limit the thumb's ability to interact with the pinkie finger. While this is not a very common grasping technique, it highlights a larger issue with this design. Implementation of the parallel-series mechanism results in a highly controllable, compact finger, at the expense of a larger, rigid palm. Ideally, the thumb's CMC joint would be located within the palm. This means the thumb must be moved farther away from the fingers, resulting in longer phalange lengths and reduced force transmission. The simulation also highlighted an issue with finger speed, a particularly challenging aspect of robotic hand design. As noted in the hand review, while most robotic hand designers employ their own methods for evaluating force output, few explicitly address the speed of their grasps. A lower gear ratio could be used in the motors to achieve higher speeds, but this would also decrease the force output. Alternatively, the bellcrank dimensions could be altered to prioritize speed over force transmission.

Regardless of these issues, the overall goals of both the detailed design of the finger, and the hand design were met. The hand successfully executed all targeted poses, and the detailed design of the 3-DoF finger matched the size of the other fingers. Whether or not the optimal use of this mechanism

resides in a five-fingered hand is still not clear. Perhaps their best use would be in a non-anthropomorphic gripper. There is still much work to be done on in-hand manipulation, and having a highly dexterous gripper may prove to be more important than a highly anthropomorphic one.

5.1 Future Work

While these designs are highly promising, significant work remains before a five-fingered hand can be implemented. The first step is to build and test the 3-DoF finger. Although the simulations have performed well, real-world implementation always introduces additional challenges. Currently, the only sensors integrated into the finger are the motor encoders; there is no sensorization at the joints or fingertips. Joint encoders must be added to enable kinematic feedback, and tactile sensors should be incorporated into the fingertips to provide kinetic feedback. While these additions would increase the cost, the finger contains ample internal space, so the physical size should remain unaffected. Another challenge lies in the highly irregular shape of the finger’s workspace, which complicates task-space control. Although there is extensive literature on singularity avoidance in task-space control [14, 11], no unified solution exists, and each case must be addressed individually. While Faulhaber does offer motion controllers compatible with their motors, they are prohibitively expensive (\$280 each), accounting for nearly 33% of the finger’s cost. Developing a more affordable motion controller is therefore essential to reducing the overall cost. Finally, a robust mounting interface must be designed. While robotic hands remain an active research area and are far from perfect, several high-quality, commercially available robotic arms exist [26, 43]. Designing a reliable interface to attach the hand to one of these arms is critical for conducting meaningful grasping experiments.

Bibliography

- [1] AIDIN ROBOTICS. *Miniature 6-Axis Force Torque Sensor*. URL: <https://www.aidinrobotics.co.kr/en/product-page/%EB%B3%B5%EC%A0%9C-miniature-6-axis-force-torque-sensor-exhibition-promotion>.
- [2] Nicholas Baiata. *Github - Kinematics and Simulation of 4-DoF Series-Parallel Robotic Thumb*. 2025. URL: <https://github.com/nickbe24/Thumb>.
- [3] Nicholas Baiata. *Motion Control of 4-DoF Robotic Thumb and 16-DoF Robotic Hand (Supplementary Video)*. 2025. URL: <https://youtu.be/M7MD1PZ9hUo>.
- [4] Nikola Banović et al. “Kinematic modelling and design of a tendon actuated soft manipulator”. In: *IFAC-PapersOnLine* 55.38 (2022). 13th IFAC Symposium on Robot Control SYROCO 2022, pp. 13–18. ISSN: 2405-8963. DOI: <https://doi.org/10.1016/j.ifacol.2023.01.127>. URL: <https://www.sciencedirect.com/science/article/pii/S2405896323001349>.
- [5] M. Barakat, J. Field, and J. Taylor. “The Range of Movement of the Thumb”. In: *HAND* 8 (June 2013). DOI: [10.1007/s11552-013-9492-y](https://doi.org/10.1007/s11552-013-9492-y).
- [6] Antonio Bicchi, J. Kenneth Salisbury, and David L. Brock. “Contact sensing from force measurement”. In: *International Journal of Robotics Research* 12.3 (1993), pp. 249–262.

- [7] Ian M. Bullock and Aaron M. Dollar. “Classifying Human Manipulation Behavior”. In: *2011 IEEE International Conference on Rehabilitation Robotics (ICORR)*. Zurich, Switzerland, 2011.
- [8] Ian M. Bullock, Thomas Feix, and Aaron M. Dollar. “Analyzing Human Fingertip Usage in Dexterous Precision Manipulation: Implications for Robotic Finger Design”. In: *2014 IEEE/RSJ International Conference on Intelligent Robots and Systems (IROS 2014)*. IEEE, 2014, pp. 1622–1629. DOI: 10.1109/IROS.2014.6942748. URL: <https://ieeexplore.ieee.org/document/6942748>.
- [9] Alexander Buryanov and Viktor Kotiuk. “Proportions of Hand Segments {Proporciones de los Segmentos de la Mano}”. In: *International Journal of Morphology* 28.3 (2010), pp. 755–758.
- [10] J. Butterfass et al. “DLR-Hand II: next generation of a dexterous robot hand”. In: *Proceedings 2001 ICRA. IEEE International Conference on Robotics and Automation (Cat. No.01CH37164)*. Vol. 1. 2001, 109–114 vol.1. DOI: 10.1109/ROBOT.2001.932538.
- [11] Davide Calzolari, Roberto Lampariello, and Alessandro Massimo Giordano. “Singularity Maps of Space Robots and their Application to Gradient-based Trajectory Planning”. In: *Robotics: Science and Systems (RSS)*. Corvallis, Oregon, USA: RSS, 2020. URL: <https://www.roboticsproceedings.org/rss16/p015.pdf>.
- [12] Lillian Y. Chang and Yoky Matsuoka. “A Kinematic Thumb Model for the ACT Hand”. In: *Proceedings of the 2006 IEEE International Conference on Robotics and Automation*. IEEE. Orlando, Florida: IEEE, 2006.
- [13] Jinbao Chen and Dong Han. “The Control of Tendon-Driven Dexterous Hands with Joint Simulation”. In: *Sensors (Basel)* 14.1 (2014), pp. 1723–1739. DOI: 10.3390/s140101723.
- [14] Stefano Chiaverini, Lorenzo Sciavicco, and Bruno Siciliano. “Control of robotic systems through singularities”. In: vol. 162. Nov. 2006, pp. 285–295. ISBN: 3-540-54169-1. DOI: 10.1007/BFb0039278.

- [15] Cleveland Clinic. *Moro Reflex*. 2025. URL: <https://my.clevelandclinic.org/health/articles/moro-reflex>.
- [16] Cockrill Corporation. *Rod Ends & Ball Joint - Miniature Nickel Silver*. 2025. URL: <https://cockrillcorp.com/products/rod-ends-ball-joint-miniature-nickel-silver>.
- [17] Shadow Robot Company. *How Much Does a Robot Hand Cost?* <https://www.shadowrobot.com/blog/how-much-does-a-robot-hand-cost/>. Accessed: 2025-03-06.
- [18] Shadow Robot Company. *Shadow Dexterous Hand: Technical Specification*. Tech. rep. © Shadow Robot Company 2024. All rights reserved. Shadow Robot Company, 2024.
- [19] Mark Cutkosky. “On grasp choice, grasp models, and the design of hands for manufacturing tasks”. In: *Robotics and Automation, IEEE Transactions on* 5 (July 1989), pp. 269 –279. DOI: 10.1109/70.34763.
- [20] Brice Denoun. *How, where and why are researchers using the Shadow Dexterous Hand?* Published on Shadow Robot’s website. 2021. URL: <https://www.shadowrobot.com>.
- [21] Ashish D Deshpande et al. “Control strategies for the index finger of a tendon-driven hand”. In: *The International Journal of Robotics Research* 32.1 (2013), pp. 115–128. DOI: 10.1177/0278364912466925. URL: <https://doi.org/10.1177/0278364912466925>.
- [22] Y. Elsayed et al. “Finite element analysis and design optimization of a pneumatically actuating silicone module for robotic surgery applications”. In: *Soft Robotics* 1.4 (2014), pp. 255–262.
- [23] Robot Era. *XHAND1 Robotic Dexterous Hand*. 2024. URL: <https://www.robotera.com/en/goods1/4.html>.
- [24] FAULHABER. *08LSL Series Motors*. 2025. URL: <https://www.faulhaber.com/en/products/series/08ls1/#34151>.
- [25] D. J. Giurintano et al. “A virtual five-link model of the thumb”. In: *Medical Engineering & Physics* 17 (1995), pp. 297–303.

- [26] Franka Emika GmbH. *Franka Research 3*. <https://franka.de/products/franka-research-3>. 2024.
- [27] IKO International. *Ball-Type Linear Motion Rolling Guides*. 2025. URL: <https://ikont.com/linear-guides/ball-type-linear-motion-rolling-guides/>.
- [28] A. Kapandji. “Cotation clinique de l’opposition et de la contre-opposition du pouce”. In: *Annales de Chirurgie de la Main* 5.1 (1986), pp. 67–73. ISSN: 0753-9053. DOI: [https://doi.org/10.1016/S0753-9053\(86\)80053-9](https://doi.org/10.1016/S0753-9053(86)80053-9). URL: <https://www.sciencedirect.com/science/article/pii/S0753905386800539>.
- [29] S. Reza Kashef, Samane Amini, and Alireza Akbarzadeh. “Robotic hand: A review on linkage-driven finger mechanisms of prosthetic hands and evaluation of the performance criteria”. In: *Mechanism and Machine Theory* 145 (2020), p. 103677. ISSN: 0094-114X. DOI: <https://doi.org/10.1016/j.mechmachtheory.2019.103677>. URL: <https://www.sciencedirect.com/science/article/pii/S0094114X19322839>.
- [30] Uikyum Kim et al. “A Novel Intrinsic Force Sensing Method for Robot Manipulators During Human-Robot Interaction”. In: *IEEE Transactions on Robotics* (2021).
- [31] Uikyum Kim et al. “Integrated linkage-driven dexterous anthropomorphic robotic hand”. In: *Nature Communications* 12 (2021), p. 7177. DOI: [10.1038/s41467-021-27261-0](https://doi.org/10.1038/s41467-021-27261-0).
- [32] Sven Lilge et al. “Tendon Actuated Continuous Structures in Planar Parallel Robots: A Kinematic Analysis”. In: *Journal of Mechanisms and Robotics* 13.1 (Dec. 2020), p. 011025. ISSN: 1942-4302. DOI: [10.1115/1.4049058](https://doi.org/10.1115/1.4049058). eprint: https://asmedigitalcollection.asme.org/mechanismsrobotics/article-pdf/13/1/011025/6611490/jmr_13_1_011025.pdf. URL: <https://doi.org/10.1115/1.4049058>.
- [33] Hongbin Liu et al. “Finger contact sensing and the application in dexterous hand manipulation”. In: *Autonomous Robots* 39 (2015), pp. 25–41.

- [34] Jixiao Liu et al. “Cost-Efficient Flexible Supercapacitive Tactile Sensor With Superior Sensitivity and High Spatial Resolution for Human-Robot Interaction”. In: *IEEE Access* 8 (2020), pp. 64836–64845. DOI: 10.1109/ACCESS.2020.2984511. URL: <https://ieeexplore.ieee.org/document/9051698/>.
- [35] Ya-Feng Liu, Wei Wang, and Xu-Fang Chen. “Progress and prospects in flexible tactile sensors”. In: *Frontiers in Bioengineering and Biotechnology* 11 (2023). DOI: 10.3389/fbioe.2023.1264563. URL: <https://www.frontiersin.org/articles/10.3389/fbioe.2023.1264563/full>.
- [36] Kevin M. Lynch and Frank C. Park. *Modern Robotics: Mechanics, Planning, and Control*. Cambridge, UK: Cambridge University Press, 2017, pp. 219–221. ISBN: 9781107156302. URL: http://hades.mech.northwestern.edu/index.php/Modern_Robotics.
- [37] Raymond R. Ma and Aaron M. Dollar. “On Dexterity and Dexterous Manipulation”. In: *Proceedings of the 2011 International Conference on Advanced Robotics (ICAR)*. 2011, pp. 196–203. URL: https://www.eng.yale.edu/grablab/pubs/Ma_ICAR2011.pdf.
- [38] Maxon Group. *ECX SPEED Brushless DC Motors*. 2025. URL: https://www.maxongroup.us/maxon/view/category/motor?etcc_cu=onsite&etcc_med_onsite=Product&etcc_cmp_onsite=ECX+SPEED+Programm&etcc_plc=Overview-Page-brushless-DC-Motors&etcc_var=%5bch%5d%23de%23_d_&target=filter&filterCategory=ECX.
- [39] McMaster-Carr. *McMaster-Carr Industrial Supply*. 2025. URL: <https://www.mcmaster.com/>.
- [40] Visakha Nanayakkara et al. “The Role of Morphology of the Thumb in Anthropomorphic Grasping: A Review”. In: *Frontiers in Mechanical Engineering* 3 (2017), p. 5. DOI: 10.3389/fmech.2017.00005. URL: <https://www.frontiersin.org/articles/10.3389/fmech.2017.00005/full>.
- [41] Keung Or et al. “A Study on Fingertip Designs and Their Influences on Performing Precision Grasping and Manipulation Tasks”. In: *2016 IEEE/RSJ International Conference on Intelligent Robots and Sys*

- tems (IROS)*. IEEE, 2016, pp. 2836–2841. DOI: 10.1109/IROS.2016.7803361. URL: <https://ieeexplore.ieee.org/document/7803361>.
- [42] American Academy of Orthopaedic Surgeons. *Finger Fractures*. 2025. URL: <https://orthoinfo.aaos.org/en/diseases--conditions/finger-fractures/>.
 - [43] Kinova Robotics. *Gen3 Robots*. <https://www.kinovarobotics.com/product/gen3-robots>. 2024.
 - [44] Wonik Robotics. *Allegro Hand V4*. 2024. URL: <https://www.allegrohand.com/ah-v4>.
 - [45] Kenneth Shaw, Ananye Agarwal, and Deepak Pathak. “LEAP Hand: Low-Cost, Efficient, and Anthropomorphic Hand for Robot Learning”. In: *Robotics: Science and Systems (RSS 2023)*. Daegu, Republic of Korea: Carnegie Mellon University, 2023. URL: <https://www.roboticsproceedings.org/rss19/p089.pdf>.
 - [46] Tessolo. *DG-5F*. <https://en.tesollo.com/dg-5f/>. Accessed: 2025-03-06.
 - [47] Yuyang Wei et al. “Fully 3D printed flexible, conformal and multi-directional tactile sensor with integrated biomimetic and auxetic structure”. In: *Communications Engineering* 2.1 (2023), p. 80. DOI: 10.1038/s44172-023-00131-x. URL: <https://www.nature.com/articles/s44172-023-00131-x>.
 - [48] D. E. Whitney. “Resolved Motion Rate Control of Manipulators and Human Prostheses”. In: *IEEE Transactions on Man-Machine Systems* 10.2 (1969), pp. 47–53.
 - [49] P.K. Wright, J.W. Demmel, and M.L. Nagurka. “The Dexterity of Manufacturing Hands”. In: *ASME Winter Annual Meeting*. San Francisco, CA, 1989, pp. 157–163.
 - [50] Licheng Wu, Yanxuan Kong, and Xiali Li. “Review and Research Issues on Underactuated Finger Mechanism”. In: *Lecture Notes in Electrical Engineering* 338 (Mar. 2015), pp. 171–180. DOI: 10.1007/978-3-662-46466-3_18.

- [51] Thiha Zaw et al. “Design and Kinematic Analysis of a Novel Series-Parallel Hybrid Finger for Robotic Hands”. In: *Journal of Mechanisms and Robotics* 17.4 (2025). Published online: November 22, 2024, p. 044512. DOI: 10.1115/1.4067024.
- [52] N. Freris Zhanchi Wang Gaotian Wang. “Unified Kinematic and Dynamical Modeling of a Soft Robotic Arm by a Piecewise Universal Joint Model”. In: *CoRR* abs/2109.05791 (2021). Withdrawn. arXiv: 2109.05791. URL: <https://arxiv.org/abs/2109.05791>.